



# Engineering Applications of Computational Fluid Mechanics

ISSN: (Print) (Online) Journal homepage: [www.tandfonline.com/journals/tcfm20](http://www.tandfonline.com/journals/tcfm20)

## Impact of the train heights on the aerodynamic behaviour of a high-speed train

Kaiwen Wang, Xiaohui Xiong, Chihyung Wen, Xiaobai Li, Guang Chen, Zhengwei Chen & Mingzan Tang

To cite this article: Kaiwen Wang, Xiaohui Xiong, Chihyung Wen, Xiaobai Li, Guang Chen, Zhengwei Chen & Mingzan Tang (2023) Impact of the train heights on the aerodynamic behaviour of a high-speed train, Engineering Applications of Computational Fluid Mechanics, 17:1, 2233614, DOI: [10.1080/19942060.2023.2233614](https://doi.org/10.1080/19942060.2023.2233614)

To link to this article: <https://doi.org/10.1080/19942060.2023.2233614>



© 2023 The Author(s). Published by Informa UK Limited, trading as Taylor & Francis Group.



Published online: 13 Jul 2023.



Submit your article to this journal [↗](#)



Article views: 943



View related articles [↗](#)



View Crossmark data [↗](#)

# Impact of the train heights on the aerodynamic behaviour of a high-speed train

Kaiwen Wang<sup>a,b,c,d</sup>, Xiaohui Xiong<sup>a,b,c</sup>, Chihyung Wen<sup>d</sup>, Xiaobai Li<sup>a,b,c</sup>, Guang Chen<sup>a,b,c</sup>, Zhengwei Chen<sup>e</sup> and Mingzan Tang<sup>a,b,c</sup>

<sup>a</sup>Key Laboratory of Traffic Safety on Track (Central South University), Ministry of Education, Changsha, People's Republic of China; <sup>b</sup>Joint International Research Laboratory of Key Technology for Rail Traffic Safety, Changsha, People's Republic of China; <sup>c</sup>National & Local Joint Engineering Research Center of Safety Technology for Rail Vehicle, Changsha, People's Republic of China; <sup>d</sup>The Hong Kong Polytechnic University, Department of Aeronautical and Aviation Engineering, Kowloon, People's Republic of China; <sup>e</sup>The Hong Kong Polytechnic University, Department of Civil and Environmental Engineering, Kowloon, People's Republic of China

## ABSTRACT

The impact of train heights on train aerodynamic performance is studied by using an improved delayed detached-eddy simulation (IDDES) method. The correctness of the numerical method has been verified by the existing wind tunnel and moving model experiments data. The aerodynamic drag, lift, slipstream, and wake flow are compared for three train heights. The results presented that the drag and lift increased by 6.2% and 23.8% respectively, with an increase in train height from 3.89 m to 4.19 m. Compared with the 3.89 m case, the maximum time-averaged slipstream at the platform location for 4.04 and 4.19 m cases are increased by 2.0% and 4.3% respectively. Meanwhile, the wake topology for three cases is described and analyzed quantitatively. The downwash angle of the wake longitudinal flow is increased with the increasing train height, resulting in the mixing of the downwash flow and the ground flow in advance. The wake in the higher trains tends to develop outward and downward. Besides, the higher trains will also bring greater transient aerodynamic loads to the equipment above the train. It's recommended to shorten the maintenance period of the electrical equipment above the higher trains to ensure the devices' safety.

**Abbreviations:** CFL: Courant–Friedrichs–Lewy; COT: Center of the track; FDR: Flow development region; FFT: Fast Fourier transform; GF: Ground-fixed reference system; ICE3: Intercity Express 3; IDDES: Improved delayed detached-eddy simulation; LES: Large-eddy simulation; LV: Longitudinal vortex; MME: Moving model experiments; NBL: Negative bifurcation line; PBL: Positive bifurcation line; PSD: Power spectral density; RANS: Reynolds averaged Navier – Stokes; SF: Stable focus; SP: Saddle point; STBR: Single-track ballast and rails; SV: Spanwise vortex; TF: Train-fixed reference system; TOR: Top of the track; TSI: Technical specification for interoperability; UN: Unstable node; WPR: Wake propagation region

## ARTICLE HISTORY



Received 21 February 2023  
Accepted 17 June 2023

## KEYWORDS

Train height; aerodynamic force; slipstream; wake flow; IDDES

## Nomenclature

$C$	Length of the simulation domain	$L$	Train length
$C_1$	Distance from the head nose to the inlet	$N$	Quantity of samples
$C_2$	Distance from the tail nose to the outlet	$n$	Distance between first grid point and train wall
$C_d$	Drag force coefficient	$Re$	Reynolds number
$C_l$	Lift force coefficient	$S$	Maximum cross-sectional area of the train
$C_p$	Pressure coefficient	$St$	Strouhal number
$f$	Frequency	$T_{inf}$	Dimensionless time
$F_d$	Drag force	$u_\tau$	Friction velocity
$F_l$	Lift force	$U_{GF}$	Stream-wise normalized velocity of GF system
$G$	Height of the simulation domain	$U_{inf}$	Incoming flow speed
$H$	Train height	$\bar{U}_p$	Average peak instantaneous slipstreams
$K$	Width of the simulation domain	$U_{slipstream}$	Slipstream velocity
$l$	Vortex core height		

**CONTACT** Mingzan Tang  mingzan\_tang@163.com  Key Laboratory of Traffic Safety on the Track of Ministry of Education, School of Traffic & Transportation Engineering, Central South University, Changsha, 410075, People's Republic of China

$\bar{U}_{slipstream}$	Time-averaged slipstream
$U_{TF}$	Stream-wise normalized velocity of <i>TF</i> system
$U_{TSI}$	<i>TSI</i> slipstream
$\nu$	Kinetic viscosity
$V_{GF}$	Spanwise normalized velocity of <i>GF</i> system
$V_{TF}$	Spanwise normalized velocity of <i>TF</i> system
$w$	Vortex core width
$W$	Train width
$W_{GF}$	Vertical normalized velocity of <i>GF</i> system
$W_{TF}$	Vertical normalized velocity of <i>TF</i> system
$x^i$	An independent sample force coefficient
$\Delta l$	Stream-wise grid scale
$\Delta s$	Spanwise grid scale
$\alpha$	Angle between downwash flow and ground flow
$\rho$	Air density
$\sigma$	Standard deviation
$\mu$	Average force coefficient

## 1. Introduction

High-speed railway transportation has been highly recognized as one of the most important modes of transportation, because of its efficient and comfortable characteristics. The research on train aerodynamic characteristics has received widespread attention along with the higher operating speed of the train. For example, the aerodynamic drag of a train will account for more than 75% of the total resistance when the speed surpasses 250 km/h (Raghunathan et al., 2002). On the other hand, the transient airflow (refers as slipstream) generated by the train operation causes the instability and fall of people on the side of the track or blows away the objects close to the train, which makes people realize the important impact of improving slipstream on the safe operation of a train (Tian, 2019).

Under the above background, train-related aerodynamics topics become imperative. For drag reduction, extensive optimization of train shape is implemented to reduce aerodynamic drag. In general, the streamlined head design delays the separation of tail airflow by changing the features of the flow field around the train (Niu et al., 2018). The thickness of the boundary layer around the train decreases with the increase of the streamlined length of the train, thus producing a drag reduction effect. In addition, researchers also focused on windshield connection optimization (Cheng et al., 2022; Xia et al., 2020), pantograph sinking (Liu et al., 2022), and bogie diversion design (Wang et al., 2020). These studies show that the flow at the windshield, pantograph, and bogie will cause different degrees of separation, which is the main component of the total resistance of the train. By wrapping or

sinking the above parts, the drag reduction of the train has been further improved. This relevant literature provides a good foundation for further exploring the impact of train shape on its aerodynamic forces.

On the topic of slipstream safety, researchers have conducted numerous field experiments (Baker et al., 2014a, 2014b), moving model experiments (MME) (Bell et al., 2015), wind tunnel experiments (Zou et al., 2022) and numerical calculations (Xia et al., 2017) to understand the slipstream characteristics. Baker et al. (2014a, 2014b) proposed a method to determine the safe distance between the platform and the operation based on the 1-second average slipstream value, and studied the slipstream characteristics of different types of high-speed trains at different positions on the track or platform. It was pointed out that the maximum slipstream of the train generally occurs in the near wake region of the train. To understand the flow fields around the train, Hemida et al. (2010) found that slipstream can be divided into six main areas: upstream, nose, inter-carriage gaps, tail, wake and far wake regions. The slipstream usually experiences local velocity peaks near the train's nose and exhibits highly turbulent flow characteristics in the nose and wake regions. Moreover, Bell et al. (2017) investigated the impact of the tail roof angle on the unsteady wake structure and corresponding slipstreams. The results indicate that increasing the tail roof angle will change the basic characteristics of the wake, forcing the wake to transition from a characteristic of sinusoidal and anti-symmetric motion to an unsteady wake dominated by large-scale separation of vortices shedding from the side of the train. More recently, Wang et al. (2018) studied the effect of the bogie on the slipstream and wake around the train, and found that the bogie significantly increases the bottom flow and turbulence level of the wake, and tends to induce spanwise oscillation of the wake.

Through the above investigations, the flow field structure and dynamic characteristics around the train, especially the train boundary layer and wake region, are the main objectives of the study of aerodynamic forces and slipstream. Recently, the capacity of some railway lines has gradually become saturated. In addition to the topic of train drag and slipstream, the improvement of transportation capacity has to be considered. Generally, the line capacity can be increased by reducing the departure interval (Wang et al., 2022), increasing the marshalling length (Tan et al., 2020), or adopting a double-unit train (Guo et al., 2020). However, these strategies are easily limited by the railway signal system and the platform length. The alternative method is to use duplex-decker trains (DDT), which set the layout of upper and lower seats by increasing the height of the train. For example, the passenger capacity of French TGV duplex-decker trains is about 45% higher than that of single-decker

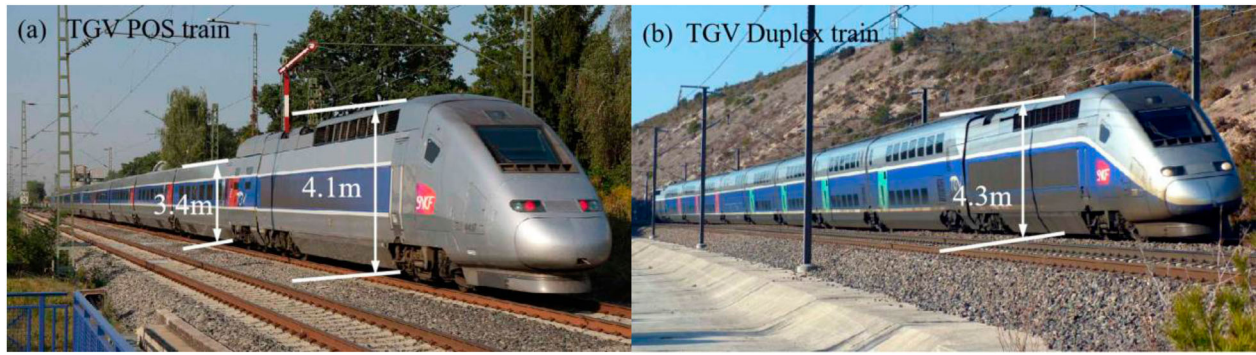


**Figure 1.** Single-decker train and duplex-decker train: (a). TGV POS (Paris-Ostfrankreich-Süddeutschland) train and (b) TGV Duplex train. For more parameter details of the models, please refer to Masson et al. (2012) and Paradot and Bouchet (2009).

TGV (as shown in Figure 1). Hence, DDT is gradually popularized in some countries due to its advantages in passenger capacity. The current work attempts to discuss the aerodynamic behaviour of DDT, rather than from the perspective of passenger capacity or energy efficiency.

In fact, the study of DDT aerodynamic characteristics is similar to that of double-decker buses (François et al., 2009), except that their shape and Reynolds number are different. In high-performance car racing, car height also has a great impact on vehicle maneuvering performance. Generally, a lower body and chassis will reduce the drag coefficient and provide greater down-force, thereby improving the stability and maneuvering performance of the vehicle (Aschwanden et al., 2009; Mohrfeld-Halterman & Uddin, 2016). But DDT's scheme objective seems to be contrary to that of high-performance cars, with the former paying more attention to the passenger transport capacity. Overall, geometric profile is a major factor affecting the aerodynamic characteristics of the train, including the aforementioned streamlined head, train formation length, and other factors. The research on the appearance of these trains mainly focuses on the overall aspect ratio and local structural optimization of the trains. However, there is no relevant research on the changes in train height, which will directly affect the height-to-width aspect ratio of the train section and tail slant angle. The factor of slant angle have been systematically studied in many Ahmed body documents (Siddiqui & Agelin-Chaab, 2022). It will directly affect the flow state behind the tail, and even change the critical point of its aerodynamic force. Therefore, under the different slant angles, the train wake states, and the associated aerodynamic forces are also more worthy of in-depth discussion. Additionally, the potential impact of the change in the height-to-width aspect ratio on train aerodynamic force and wake flow cannot be ignored.

The current work aims to explore the impact of train heights on its aerodynamic behaviour, especially aerodynamic drag and lift, slipstream, and wake flow.

The rest of the article is organized as follows. Section 2 contains train models, simulation domain and boundary conditions, grid setup, solution method, and verification of calculation method. The aerodynamic drag and lift force, the influence of train height on slipstream, and the comparison of the wake flow are described in section 3. The safety analysis is discussed in section 4. Concluding remarks are provided in section 5.

## 2. Methodology

### 2.1. Train models

The current work utilized the 1/10th 3-car formation German Intercity Express 3 (ICE3) train, which is widely used in Europe and Asia. The position of the train and single-track ballast and rails (STBR) are shown in Figure 2(a), and the dimensions are following CEN guidelines (CEN European Standard, 2013). The original ICE3 width is  $W = 294$  mm, which is specified as the reference length. The length ( $L$ ) and height ( $H$ ) of the train are  $L = 26 W$  and  $H = 1.32 W$  respectively. The wiper, air conditioner, and pantograph are ignored in the simulation model, and the bogie part is simplified. As shown in Figure 1, the main difference between single – and duplex-decker trains is the change in train height. However, due to the railway clearance, the highest train is generally below 4.3 m. Thus, the heights of the three trains 389, 404, and 419 mm are chosen in the current work. Figure 2(b) shows the side elevation of the trains with different heights. To study the effects of the height-to-width aspect ratio and the tail slant angle on aerodynamic behaviour, the parts below the nose height of the trains are the same. Other shape parameters, including head shape, bogie structure and clearance between compartments and train length, remain unchanged. To facilitate researchers in reproducing the model, only the main profile of the train above the nose height is proportionally enlarged vertically. Meanwhile, the top view shape is the same to keep the basic features of the model



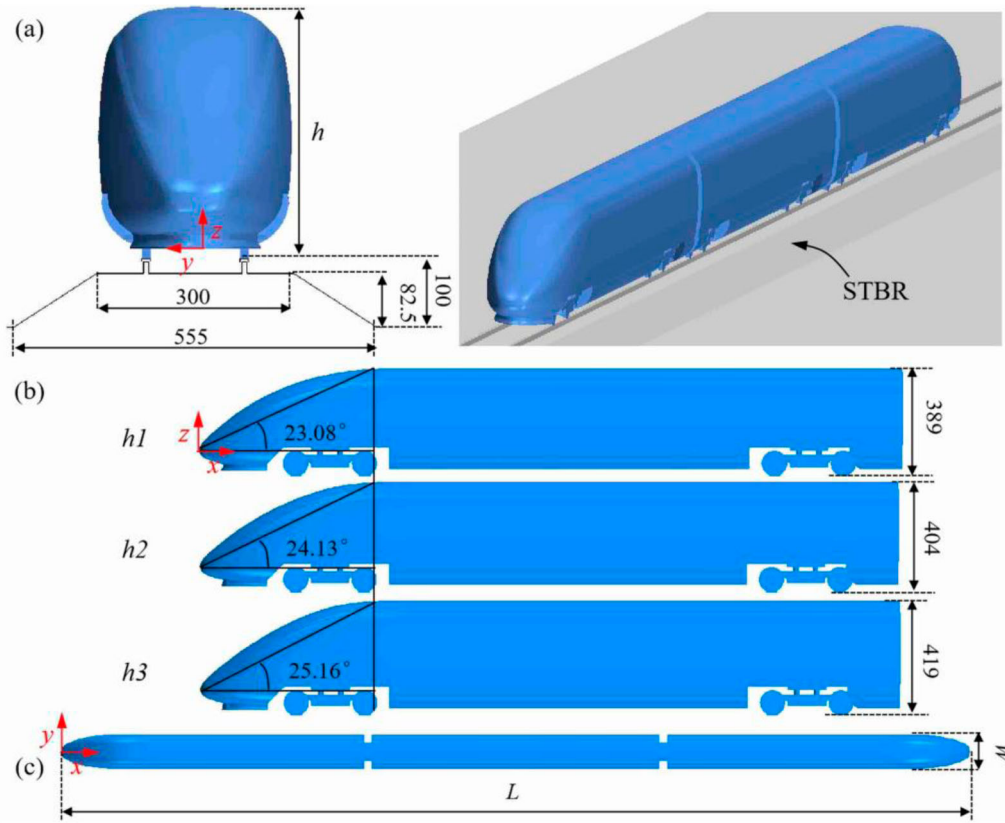


**Figure 2.** Train models: (a) front and overall elevation, (b) side elevation, and (c) vertical view (unit: mm).

consistent (see Figure 1(c)). For the sake of description, we name these three different height configurations  $h1$ ,  $h2$ , and  $h3$  respectively. The following sections 2.2 to 2.5 are all analyzed with  $h1$ .

## 2.2. Simulation domain and boundary conditions

The train is installed in a  $76W$  (length)  $\times 40W$  (width)  $\times 20W$  (height) cuboid domain with a blockage ratio of 0.15%, see Table 1 and Figure 3. The boundary of incoming flow is the velocity inlet, and the outlet is set as a zero-pressure gradient boundary to reduce the impact of the outlet on the upstream flow field. The incoming flow speed ( $U_{inf}$ ) is 13.8 m/s and the Reynolds number based on the width is  $Re = 2.68 \times 10^5$ . The reason for choosing this value is to facilitate comparison with the moving-model experiment and reduce the computing resources. Meanwhile, the Reynolds number of the current work is higher than the minimum value of  $2.5 \times 10^5$  proposed by the CEN standard (CEN European Standard,

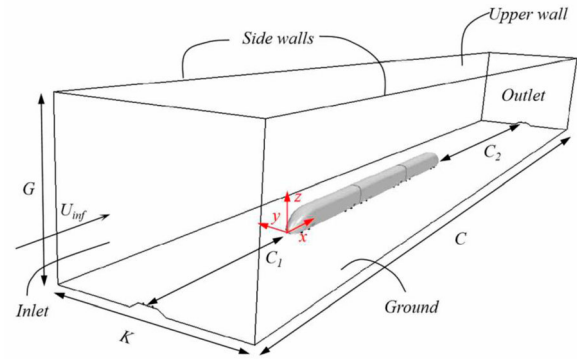


**Figure 3.** Schematic diagram of calculation domain and boundary.

2013), which means the full-scale trains' slipstream characteristics can be correctly captured by the reduced-scale experiments. For subsequent numerical calculation verification, the model and Reynolds number in the current work are the same as the previous MME test (Bell et al., 2015). Besides, the top and two sides are symmetrical planes. The ground effect is considered in this work to restore the real operation scenario (Wang et al., 2018; Xia et al., 2017). The ground is set with a tangential speed of 13.8 m/s to simulate the relative movement between the train and the ground.

**Table 1.** The geometric size of the calculation domain and the train.

H	L	C	C <sub>1</sub>	C <sub>2</sub>	K	G
1.32W	26W	76W	15W	35W	40W	20W

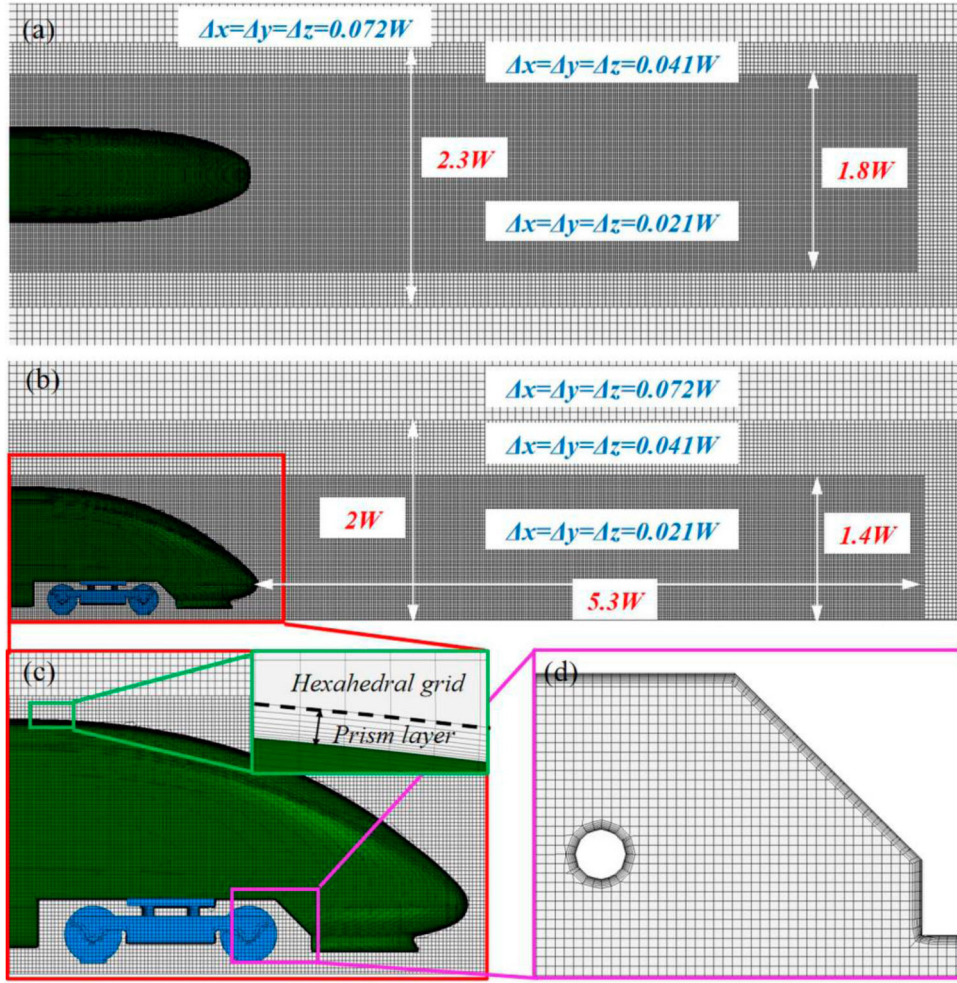


**Figure 4.** The specific distribution of the medium grid: (a) vertical view and (b) lateral view. Grids details of the prism layers: (c) train upper surface and (d) bogie surface.

### 2.3. Grid setup

The computational grid is a Cartesian grid dominated by hexahedrons. This grid technology supports the rapid generation of grids of complex geometric surfaces and can flexibly adjust the resolution of local grids. To accurately solve the turbulence near the train, one encrypted box is concentrated near the train, and the other finer encryption box is concentrated near the tail train (see Figure 4(a) and (b)). To accurately capture the airflow law in the boundary layer of the train, 15 prism layers are set on the body surface, and the growth rate of the prism layer is 1.2, shown in Figure 4 (c) and (d). Moreover, three sets of grids (i.e. coarse grid, medium

grid, and fine grid) are utilized to detect grid independence. The three group grids are only different in spatial resolution, and the prism layer grids are still consistent. As listed in Table 2,  $n^+ = u_\tau n/\nu$ ,  $\Delta l^+ = u_\tau \Delta l/\nu$ ,  $\Delta s^+ = u_\tau \Delta s/\nu$ , where  $u_\tau$  is the friction velocity,  $n$  is the distance between the first grid point and the train wall,  $\Delta l$  and  $\Delta s$  are the grid scale in the stream-wise and spanwise directions, and  $\nu$  is the kinetic viscosity. The number of fine, medium, and coarse grids is 64, 47, and 26 million respectively.

### 2.4. Solution method

The numerical simulation is completed in the software STAR-CCM + 14.02. An improved delayed detached-eddy simulation (IDDES) method based on the SST model is used to solve the turbulent flow around the train (Xia et al., 2017). The numerical simulation is based on the implicit unsteady incompressible finite volume solver. A SIMPLE algorithm is used for the pressure-velocity

**Table 2.** Setting strategy of grid spatial scale for the  $h1$  case.

Grids	$n_{mean}^+$	$n_{max}^+$	$\Delta s_{mean}^+$	$\Delta s_{max}^+$	$\Delta l_{mean}^+$	$\Delta l_{max}^+$	Size
Coarse	< 1.0	2.2	< 150	340	< 150	340	26 million
Medium	< 1.0	2.2	< 110	220	< 110	220	47 million
Fine	< 1.0	2.2	< 80	160	< 80	160	64 million

coupling treatment, and the mixed scheme is used for the discretization of the convection term. The central bounded difference scheme is used in the Large-eddy simulation (LES) region and the second-order upwind scheme is used in the Reynolds averaged Navier – Stokes (RANS) region. The turbulence and diffusion term adopt the second-order upwind scheme, and the time step adopts the second-order implicit scheme (Cheng et al., 2022). The discrete time steps are  $0.021T_{inf}$ ,  $0.01T_{inf}$ , and  $0.006T_{inf}$  (where  $T_{inf} = W/U_{inf}$  is dimensionless time) for the coarse, medium, and fine grid. The time step ensures that the Courant–Friedrichs–Lewy (CFL) number of 99% grid cells is less than 1, and the maximum CFL number is 1.2. The initialization of the calculation is performed by the steady-state RANS to make the flow field stable. Correspondingly, the initialization time is  $t = 50T_{inf}$ . Thereafter, the information of the flow field and train load data is recorded from  $50T_{inf}$  to  $400T_{inf}$ .

## 2.5. Verification of calculation method

Slipstream, wake velocity, and force coefficient are used to check the correctness of the calculation method and grid independence. Generally, the trackside and platform location, at 3 m from the centre of the track (COT) and 0.2 and 1.4 m above the top of the track (TOR) (CEN European Standard, 2013), is sampled for evaluating the time-averaged slipstream ( $\bar{U}_{slipstream}$ ). The train is running on the fixed ground in actual operation environment. But the train-fixed (TF) reference system is employed to replace the ground-fixed (GF) system in the simulation. Therefore, the velocity obtained by TF should be switched to the GF via Eq. (1) and (2). The definition of slipstream velocity ( $U_{slipstream}$ ) in current work is consistent with method published by S. Wang et al., (2020), which is defined as Eq. (3).

$$U_{GF} = 1 - \frac{U_{TF}}{U_{inf}} \quad (1)$$

$$V_{GF} = \frac{V_{TF}}{U_{inf}} \quad (2)$$

$$U_{slipstream} = \sqrt{U_{GF}^2 + V_{GF}^2} \quad (3)$$

$$W_{GF} = \frac{W_{TF}}{U_{inf}} \quad (4)$$

where  $U_{GF}$ ,  $V_{GF}$ , and  $W_{GF}$  are stream-wise, spanwise, and vertical normalized velocities based on the GF. The corresponding  $U_{TF}$ ,  $V_{TF}$ , and  $W_{TF}$  based on the TF are normalized with the incoming velocity ( $U_{inf}$ ).

The time-average slipstream at trackside and platform locations for the three grids is presented in Figure 5 (a)

and (b). The coarse grid results present obvious differences in the wake propagation region (WPR) with the other two grids. This inconsistency may be due to the coarse grid cannot accurately solve the turbulent flow around the train. However, the medium grid has sufficient grid resolution and is consistent with the slipstream of the fine grid. Figure 5 (c) presents the spanwise velocity ( $\bar{U}_{TF}$ ) distribution in WPR predicted by different grids. The spanwise lines are sampled at  $0.33W$  above the TOR,  $x = 1W$  from the tail nose. The current study found that the coarse grid cannot capture the wake flow with high turbulence. However, the wake can be resolved well with medium grid resolution. Figure 5(d) indicates the comparison of force coefficients predicted by three grids. The force coefficients are defined by Eq. (5) and (6), where  $F_d$  is the drag force and  $F_l$  is the lift force,  $\rho$  is the air density and  $S$  is the maximum cross-sectional area of the train. For the *h1* case,  $S = 0.0975\text{m}^2$ . The prediction error of the lift coefficient is larger than the drag coefficient. But compared with the fine grid, the differences in drag and lift coefficient are less than 1% at the medium grid. From the above analysis, the medium grid shows sufficient calculation accuracy for the side flow, wake flow, and aerodynamic force.

$$C_d = F_d / (0.5\rho U_{inf}^2 S) \quad (5)$$

$$C_l = F_l / (0.5\rho U_{inf}^2 S) \quad (6)$$

Another work is to verify the accuracy of train pressure distribution and slipstream with experimental data. First, the simulated pressure distribution of the upper surface centreline of the train is verified by experimental data measured by (Xia et al., 2017). The CRH3 in the experiment is basically the same as ICE3. The Reynolds number in the current work is slightly less than that in experiments ( $1.65 \times 10^6$ ). As shown in Figure 6, the simulated train surface pressure amplitude is basically consistent with the data measured in the test. However, there are wipers and air conditioning structures in the experiment, which are ignored in the calculation model. Therefore, the difference between the dotted box part and the position close to the air conditioner is relatively obvious. In general, IDDES simulation can accurately predict the body surface pressure of the train.

The slipstream is used for further comparative study to verify simulation accuracy. The ensemble-averaging method of slipstream designated by the CEN standard (CEN European Standard, 2013) has been extensively employed in slipstream analysis. To restore the transient slipstream effect during a full-scale test or dynamic model test, the moving-point method proposed by Muld et al. (2014) is adopted. Several probes shall be set at the position of trackside and platform height. When the



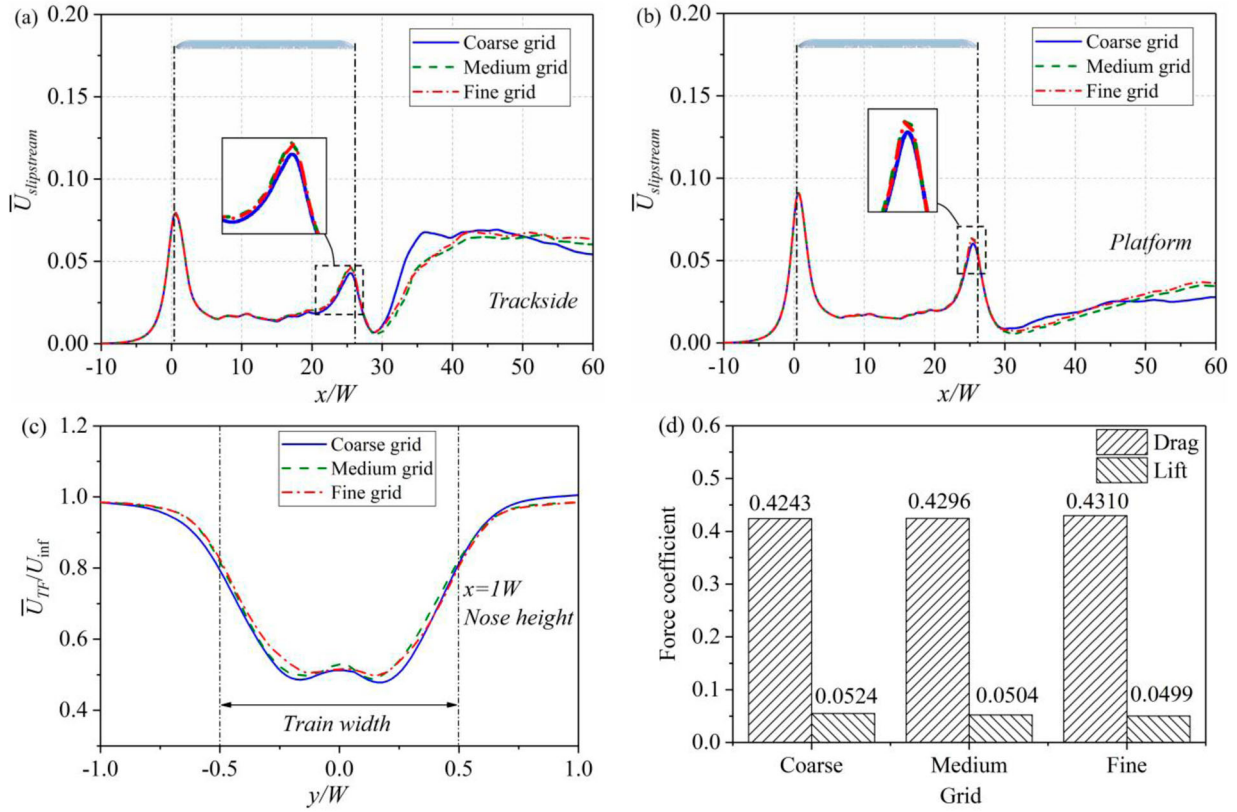


**Figure 5.** Comparison of calculation data for three grids: (a) time-average slipstream at the trackside location, (b) time-average slipstream at platform location, (c) time average velocity behind the train, and (d) aerodynamic drag and lift coefficient.

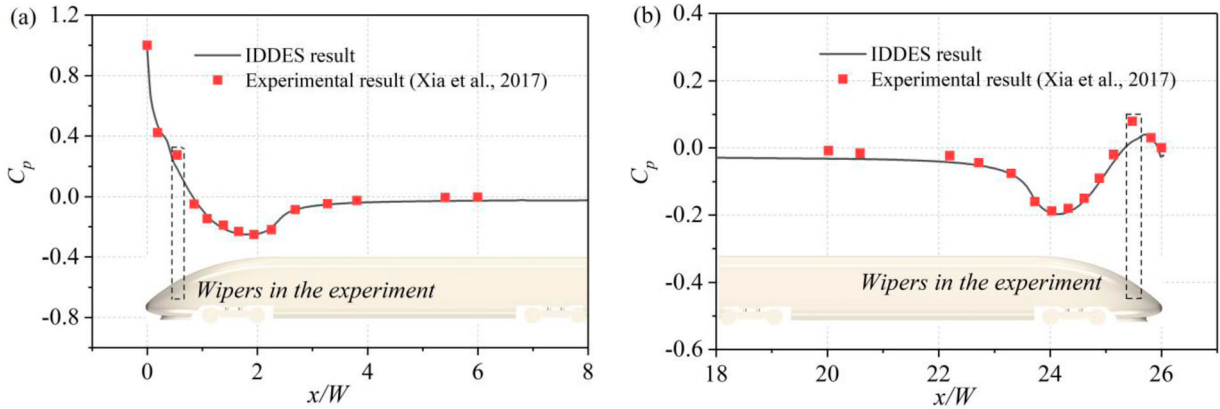


**Figure 6.** Verification of pressure coefficient ( $C_p$ ) of the upper surface centreline of train: (a) head train and (b) tail train.

flow field is stable enough, that is, the numerical simulation time reaches  $50 T_{inf}$ , a total number of 26 probes move from upstream to downstream at  $U_{inf}$  speed. This method is equivalent to the experimental scenario that fixed probes on the ground. The probes are spaced 20 m (full-scale) along the flow direction to ensure independence between the probes. The mean and standard deviation of 26 sets of slipstream data is used for the following comparison.

Figure 7 shows the comparison of the trackside position slipstream (assembly average and standard deviation

values) between the numerical simulation and the MME data. The MME (Bell et al., 2015) adopted a 1/25 scaled 3-car formation ICE3 model. The Reynolds numbers for moving model tests 1 and 2 are  $2.5 \times 10^5$  and  $3.3 \times 10^6$  respectively. To compare IDDES and MME data more conveniently, the whole train length ( $L$ ) is used for positioning alignment. As shown in Figure 7 (a), the slipstream velocity increases rapidly and generates a peak near the head nose. Then there is a flow development region ( $FDR$ ), where the slipstream speed decreases and gradually increases along the body, and forms a second



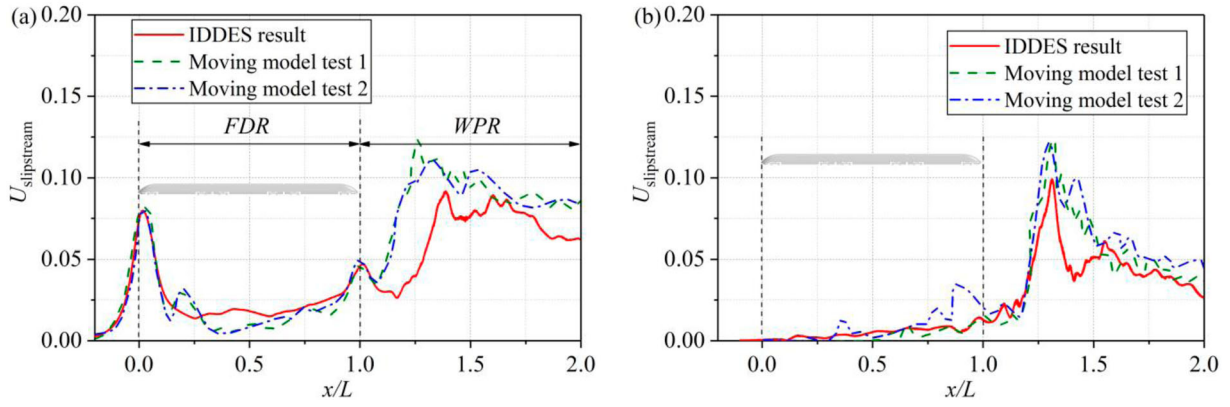


**Figure 7.** Slipstream verification at trackside location: (a) assemble-averaged slipstreams and (b) the curves of the standard deviation.

peak at the tail nose. Then there is the relatively significant wake propagation region, and the slipstream produces maximum value in *WPR*. In general, IDDES simulation accurately captures the peak value near the head train and tail train, and both differences are less than 3.1%. However, the MME is completed in an indoor confined space, while IDDES operates in a relatively larger air domain. These results present a higher slipstream peak of MME in *WPR*. However, the overall slipstream trend between the two methods is highly consistent. Overall, grid independence verification and method verification make this work choosing the IDDES model with the medium grid.

### 3. Results

#### 3.1. Aerodynamic drag and lift force

The drag and lift force of each carriage at three train heights is listed in Table 3 and Table 4. Here, the cross-sectional area of *h2* and *h3* are 0.1017 and 0.1062

m<sup>2</sup> respectively. The standard deviation ( $\sigma$ ) of force coefficients is defined as follows.

$$\sigma = \sqrt{\frac{1}{N} \sum_{i=1}^N (x^i - \mu)^2} \quad (7)$$

where  $N$  is the whole quantity of samples,  $i$  indicates an independent sample,  $x^i$  represents the force coefficient of an independent sample, and  $\mu$  is the average force coefficient.

The drag force of the tail train is the main part for three cases, followed by the head train. The  $C_d$  decreases gradually with the increase in train height, which is mainly related to the cross-sectional area. Another more intuitive comparison is force. The total  $F_d$  of *h3* is 6.2% higher than that of *h1*, which is an expected result. In terms of aerodynamic lift, the head train shows negative  $C_l$ , and the tail train has the largest  $C_l$ . When the train height increases from *h1* to *h3*, the total  $F_l$  of the train increases by 23.8%.

**Table 3.** Drag force and drag force coefficient.

Carriage	$C_d$						$F_d$ (N)		
	Mean			$\sigma$			Mean		
	<i>h1</i>	<i>h2</i>	<i>h3</i>	<i>h1</i>	<i>h2</i>	<i>h3</i>	<i>h1</i>	<i>h2</i>	<i>h3</i>
Head	0.1620	0.1588	0.1551	0.0055	0.0048	0.0051	1.8424	1.8840	1.9216
Middle	0.1016	0.1004	0.0995	0.0044	0.0039	0.0039	1.1555	1.1905	1.2330
Tail	0.1660	0.1667	0.1641	0.0084	0.0076	0.0072	1.8879	1.9775	2.0333
Total	0.4296	0.4259	0.4188	0.0182	0.0163	0.0162	4.8858	5.0520	5.1878

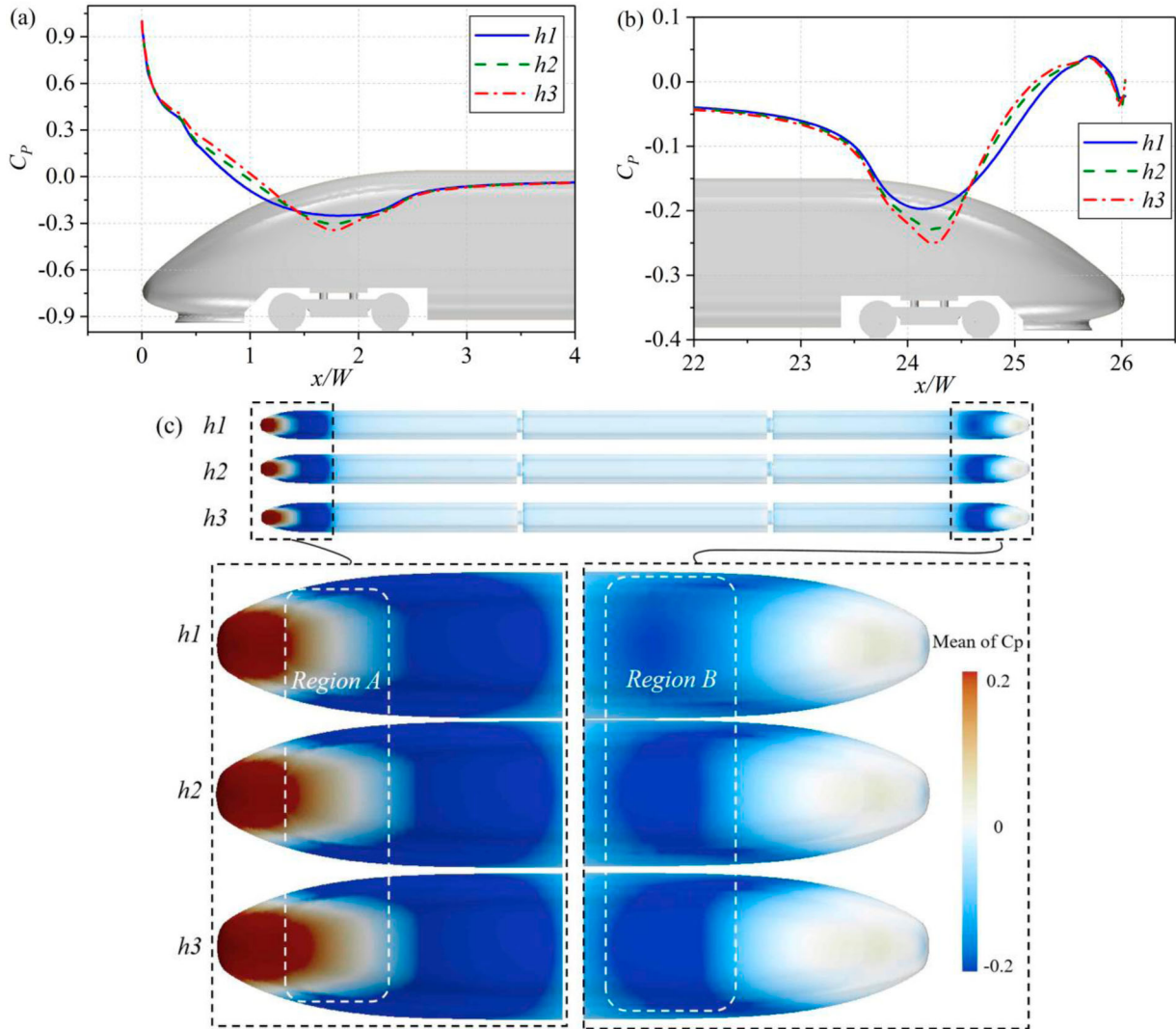
**Table 4.** Lift force and lift force coefficient.

Carriage	$C_l$						$F_l$ (N)		
	Mean			$\sigma$			Mean		
	<i>h1</i>	<i>h2</i>	<i>h3</i>	<i>h1</i>	<i>h2</i>	<i>h3</i>	<i>h1</i>	<i>h2</i>	<i>h3</i>
Head	−0.0415	−0.0419	−0.0434	0.0083	0.0060	0.0066	−0.4719	−0.4969	−0.5371
Middle	0.0019	0.0031	0.0034	0.0068	0.0060	0.0072	0.0212	0.0372	0.0417
Tail	0.0901	0.0939	0.0973	0.0116	0.0127	0.0120	1.0241	1.1143	1.2053
Total	0.0504	0.0552	0.0573	0.0267	0.0247	0.0257	0.5734	0.6546	0.7100

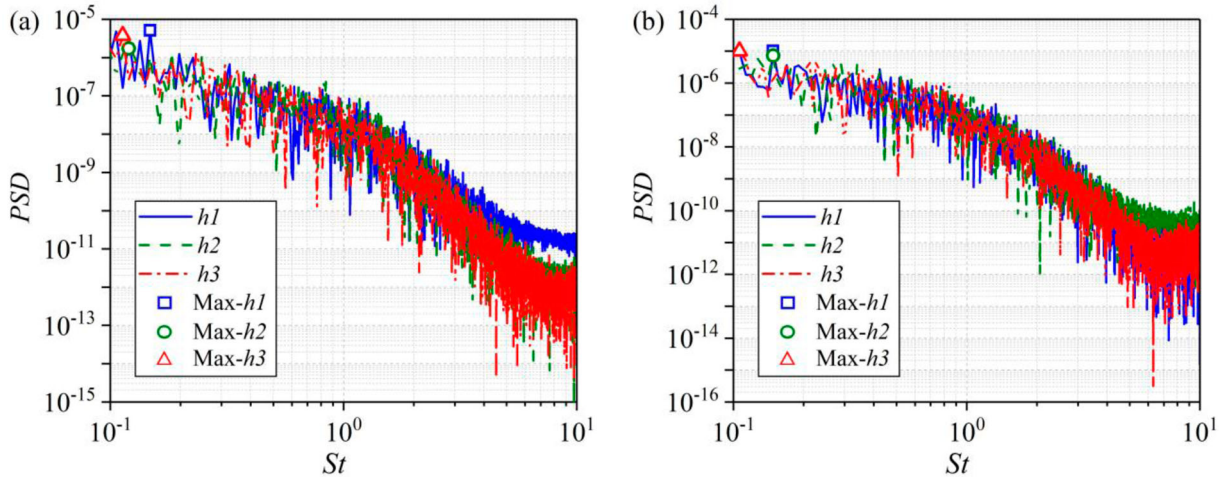
This increase in lift is an adverse factor to train operation quality. Both Table 3 and Table 4 show that the tail train has a greater aerodynamic force, and the  $\sigma$  of the tail train force is also obvious. This indicates that the force fluctuation of the tail train is relatively notable, which may be related to the shedding of the tail periodic vortex. Generally speaking, there is no obvious rule for standard deviation at different train heights. This is due to that the standard deviation mainly reflects the data change of the turbulent flow field. There may be a small deviation in the unsteady flow field.

Figure 8 indicates the pressure distribution at the upper train centreline. Generally, increasing train height will increase the slant angle of the streamlined region. The early blunt body investigation focused on the impact of shape on its aerodynamic characteristics (Ehirim et al., 2019). Additionally, the train height mainly affects the top

surface pressure. As shown in Figure 8, with the increase of head slant angle, the airflow presents a stagnation effect at the front position of the head train, increasing the pressure of  $h3$  (as shown in the area of  $0 < x/W < 1.5$  in Figure 8(a), which can also be inspected in the Region A in Figure 8(c)). Then the flow accelerates, reducing the pressure of  $h3$  (as shown in Figure 8(a)  $1.5 < x/W < 2.5$  area). In the tail streamlined region, the downwash flow of  $h3$  accelerates at the position of  $23.5 < x/W < 24.5$ , so the pressure is less than  $h1$  (this can be inspected in the Region B of Figure 8(c)). Then the pressure recovers and the pressure of  $h3$  is greater than that of  $h1$ . Therefore, from  $h1$  to  $h3$ , the increase of the positive pressure of the head train produces downward pressure, resulting in the head train obtaining a larger negative lift. Meanwhile, the larger negative pressure of the tail train produces a lifting effect. This result is consistent with the data in Table 4.



**Figure 8.** Surface pressure distribution under three train heights: (a) the pressure distributions at the upper centreline of the head train, (b) the pressure distributions at the upper centreline of the tail train, and (c) surface pressure distributions. The train is superimposed by the mean pressure coefficient.



**Figure 9.** The PSD of the tail train forces: (a) drag force coefficients, (b) lift force coefficients.

According to the standard deviation in Table 3 and Table 4, the frequency domain of tail train forces should be more deeply understood. The Fast Fourier transform (FFT) of aerodynamic force is conducted in MATLAB to obtain spectrum signals. The total duration of each force data for spectrum analysis is  $350 T_{inf}$ . In the FFT process, Hamming windowing method and 50% overlapping are used with 35000 samples per segment. Figure 9 shows the power spectral density (PSD) of the tail train force at three train heights. The frequency ( $f$ ) is normalized as Strouhal number ( $St$ ), which is defined as  $St = fW/U_{inf}$ . The power spectrum distribution will decrease with the increase of  $St$ . One explanation is that the wavelength of a vortex is shorter at high frequency, so the energy loss rate is faster (Bouferrouk, 2013). As shown in Figure 9, the PSD of aerodynamic forces at different train heights is similar, but the PSD peaks of  $h2$  and  $h3$  are weakened. The dominant frequency  $St$  of the  $h1$ ,  $h2$ , and  $h3$  drag coefficients is 0.148, 0.119, and 0.112, respectively. Correspondingly, the dominant frequency  $St$  of the  $h1$ ,  $h2$ , and  $h3$  lift coefficients is 0.148, 0.148, and 0.105 respectively. A reasonable explanation is that the higher train body has greater interference with the surrounding flow field, and the vortices near the tail train are also changed, resulting in a more scattered PSD of  $h2$  and  $h3$  and a greater slope of descent. The final result is a lower PSD peak intensity and a lower dominant frequency  $St$ .

### 3.2. The influence of train height on slipstream

#### 3.2.1. Time-averaged slipstream

The running of a high-speed train brings up airflow movement to form a slipstream, which affects facilities or people near the line with a strong transient effect. In this section, Figure 10 describes the time-average slipstream at different train heights. As shown in Figure 9,

when the probe gradually approaches the head train, the air stops at the head nose, forming a high-pressure zone, and the time-average slipstream velocity has reached the first peak. Then the slipstream drops rapidly. With the increasing boundary layer along the flow direction, the slipstream gradually increases and forms a second peak near the tail train. This phenomenon is similar to previous research conclusions (Hemida et al., 2010). The slipstream velocity behind the train will experience an increased process again. The increased train height causes severe pulsation of airflow. The free development of the detached airflow in WPR leads to the increase of the airflow pulsation, which gradually attenuates as it is far away from the tail train. The slipstream velocity of  $h2$  and  $h3$  is slightly different from that of  $h1$  in FDR, but it is greater than  $h1$  in the near wake region ( $26 < x/W < 40$ ). These relationships may partly be explained by the stronger vortex shedding from the streamline of the tail train. It's worth mentioning that compared with  $h1$ ; the heights in  $h2$  and  $h3$  also advance the appearance of the peak slipstream in WPR. This phenomenon is that the higher body produces a larger angle of downwash flow, which forces the peak to occur in advance, as shown in Figure 17 and Figure 21. Additionally, the peak slipstream increases rapidly when the probe is close to the COT.

To further understand the above slipstream phenomenon, the side flow field and boundary layer of the train are analyzed. As presented in Figure 12, the boundary layer contour line is generated along the middle of each train, which is defined as 99% of the incoming flow velocity. The  $\bar{U}$  in the figure is the synthetic velocity based on  $TF$ . It can be inspected that the train height changes the distribution of the boundary layer. First, the boundary layer of  $h2$  and  $h3$  is higher than  $h1$  as a whole. Secondly, the synthetic velocity of  $V_{TF}$  and  $W_{TF}$  in region A is also significantly higher than  $h1$ . This is consistent with

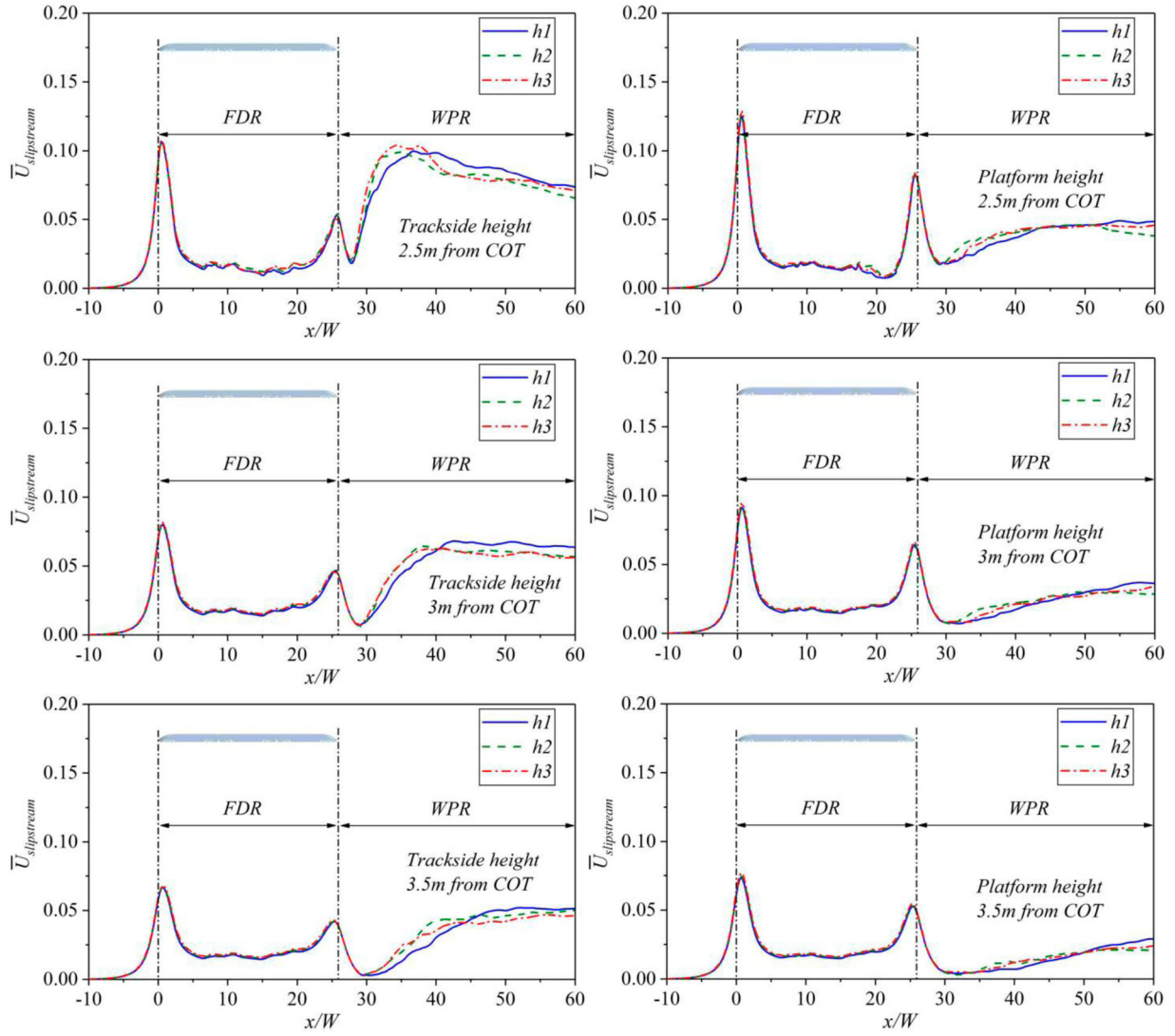


**Figure 10.** Comparison of the time-averaged slipstream along the sampled lines at 2.5, 3, and 3.5 m from the COT.

the rule in Figure 10. Because the time-averaged flow field structure on both flanks of the train is basically symmetrical, only half of the images are shown here. From the velocity distribution in the  $c3$  plane, it can be found that there are two obvious vortices above and below the skirt. When the train height increases from  $h1$  to  $h3$ , the main vortices gradually move upward and the range of the main vortices further expands. This will lead to the increase of slipstream at the mark position in the figure. As a result, a comparison of the peak time-averaged slipstream for three cases is given in Figure 11. Compared with  $h1$ , the peak slipstream of  $h2$  and  $h3$  at the trackside location is increased by 1.0% and 2.4% respectively. Furthermore, the peak slipstream at the platform location is increased by 2.0% and 4.3% respectively. These changes in slipstream velocity indicate that the higher train increases the risk of personnel and facilities near the track.

### 3.2.2. Instantaneous slipstream velocity

Instantaneous slipstream is an important content for evaluating train aerodynamic behaviour, and its measurement procedure has been described in Section 2.5. Figure 13 shows the instantaneous slipstream for all three cases. Figure 14 gives the state of the instantaneous slipstream and iso-surface at  $350T_{inf}$ . The instantaneous slipstream is displayed in the form of blue lines and the maximum value of data is marked. It can be observed that the peak instantaneous slipstream completely coincides at the head-nose position, indicating that the airflow here belongs to the laminar flow here. The cloud diagram of instantaneous slipstream velocity at  $z = 0.15W$  horizontal plane is used to explain the whole motion of the probes. Under the interference of shear unstable flow around the bogie zone, the airflow forms a highly turbulent flow with vortex structures of various scales. The high turbulent flow accelerates the energy exchange



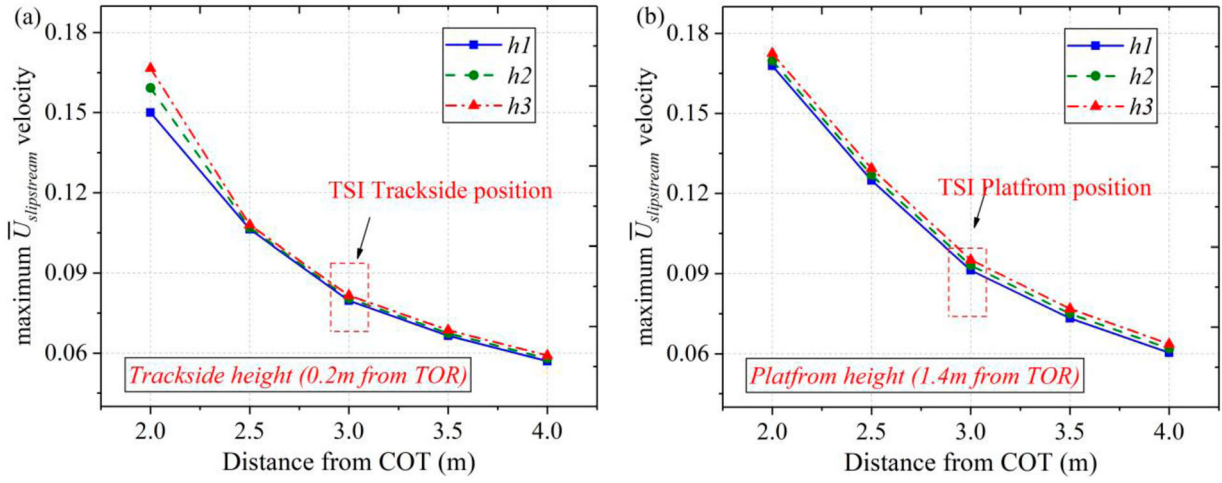


**Figure 11.** Comparison of peak time-averaged slipstreams for three cases: (a) Trackside locations, (b) Platform locations.

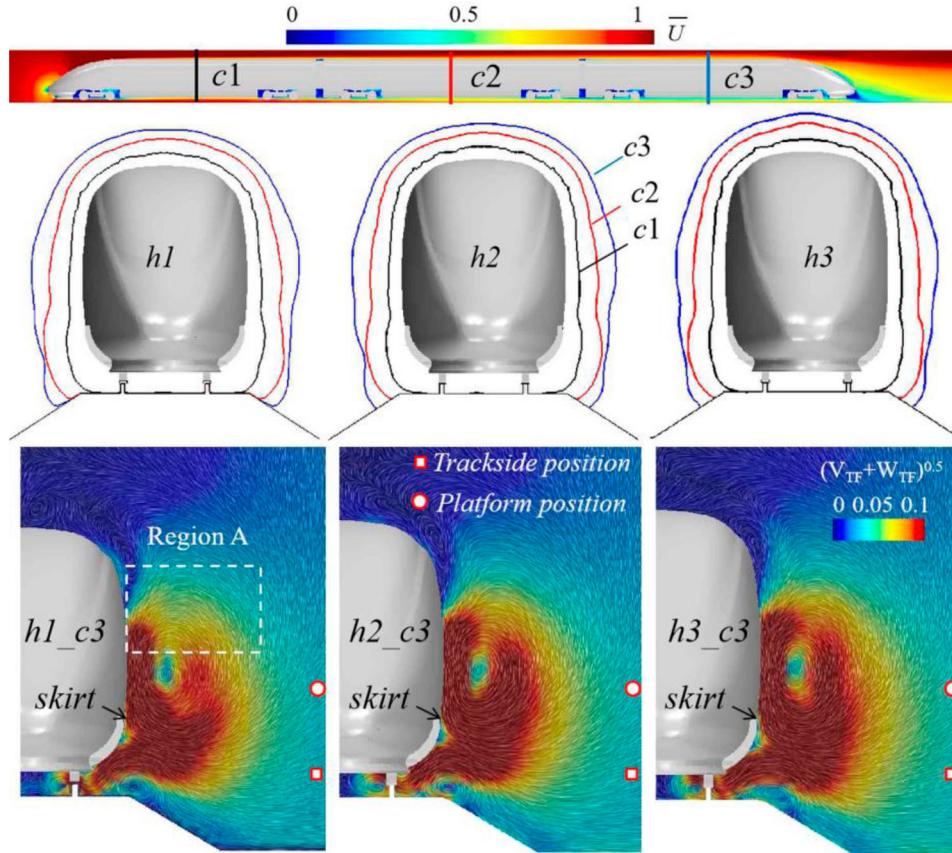


**Figure 12.** The boundary layer thickness of different sections. The sketch is coloured by mean velocity for the whole view and coloured by synthetic spanwise and vertical velocity for the cross-sections.

between the airflow around the train, and the exchange effect gradually diffuses along the flow direction with the movement of the vortex structure. Then the range of the airflow gradually expands, and the corresponding instantaneous slipstream grows. The wake flow is mixed with the side and bottom separated flow. Then wake flow develops freely to form a large-scale vortex structure

and continues to swim downward. However, the interval between large-scale vortices is the low-speed zone of the instantaneous slipstream. The lateral expansion of the vortex structure gradually moves to the location of the instantaneous slipstream probe, forming a high peak area of the instantaneous slipstream. The velocity of the vortex system is not exactly equal to that of the

train, so the probe will not always be in a certain vortex structure and will not always be in the low-speed region between the vortex systems. Therefore, the collected instantaneous slipstream value changes with the relative position of the probe and the tail vortex structure, which is shown in Figure 13. Although the instantaneous slipstream can reach 0.36 in *WPR*, the average value is far less than the maximum level.

In the real scene, the instantaneous slipstream velocity in Figure 13 cannot represent the feeling of the static observer. This work adopts the 1s-average moving value (Baker et al., 2014a, 2014b), i.e. the equivalent full-size 13.8 m window for sliding average processing. The Technical specification for interoperability (TSI) slipstream

( $U_{TSI}$ ) is defined as Eq. (8).

$$U_{TSI} = \bar{U}_p + 2\sigma \quad (8)$$

where  $\bar{U}_p$  indicates the average values of the peak instantaneous slipstreams, and  $\sigma$  indicates the standard deviation of all peak instantaneous slipstreams.

Figure 15 shows 1s-average instantaneous slipstream curves for three cases. The  $\bar{U}_p$  and  $\sigma$  values calculated in the 26 probes for three cases are shown in Table 5. In the *FDR* part, the  $\sigma$  of the instantaneous slipstream can be almost ignored. However, in the *WPR* part, the  $\sigma$  is significantly increased, which indicates that the instantaneous slipstream oscillation in the wake region is notable. Additionally, the  $U_{TSI}$  without the 1s-average method is about

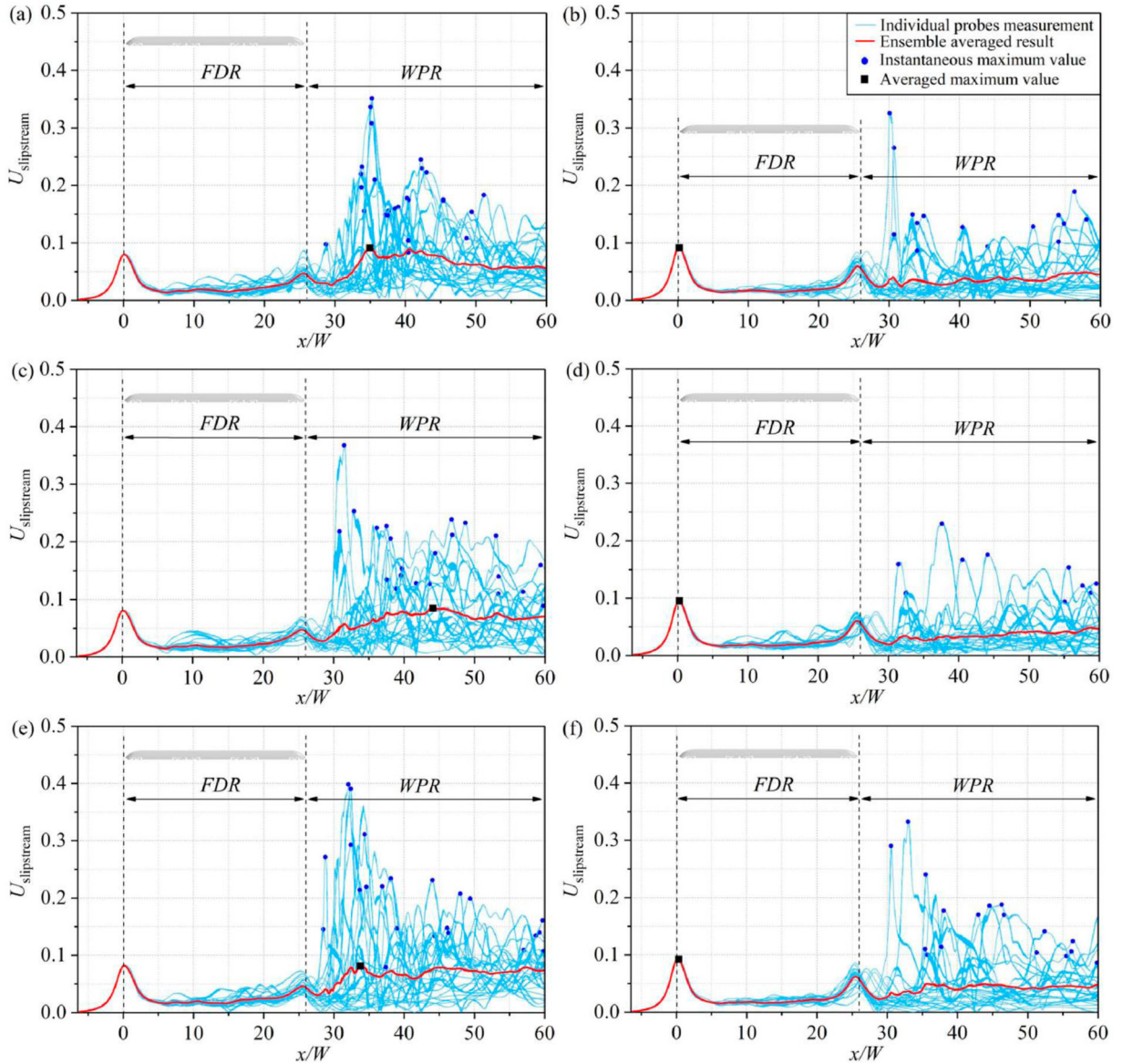


**Figure 13.** Instantaneous slipstreams. h1: (a) trackside location and (b) platform location. h2: (c) trackside location and (d) platform location. h3: (e) trackside location and (f) platform location.

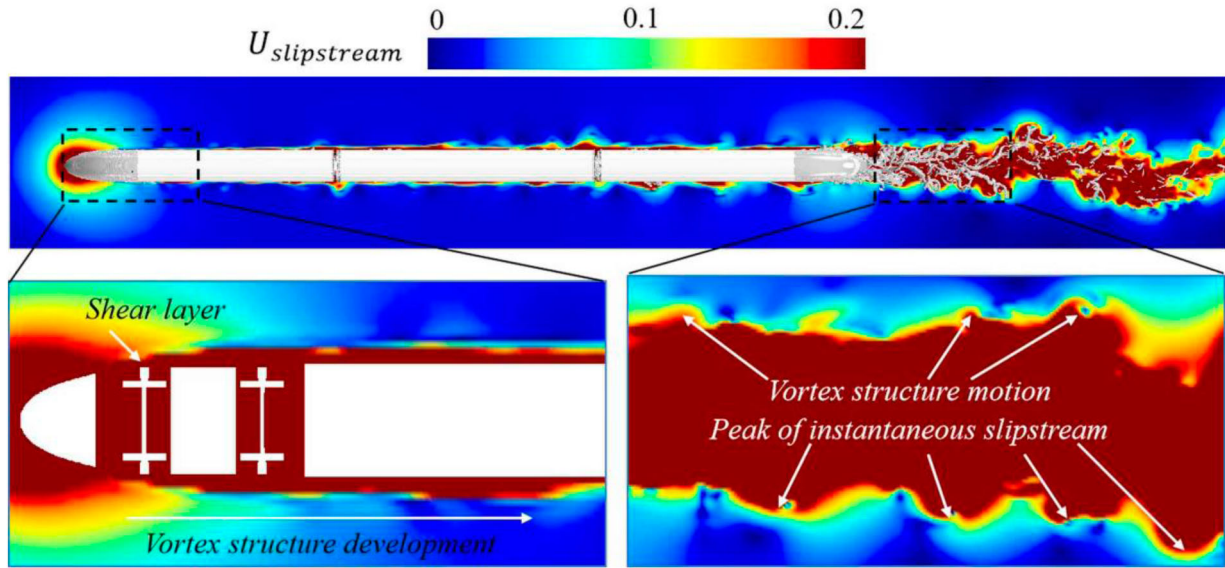


**Figure 14.** Schematic diagrams of instantaneous slipstream and iso-surfaces ( $Q = 10000$ ) of  $z = 0.15W$  plane. The photograph is recorded at  $350T_{inf}$ .

50% higher than that with the 1s-average method. This indicates that the 1s-average method is suitable for evaluating the instantaneous slipstream. Furthermore, the  $U_{TSI}$  value of the  $h3$  case is still the highest. Compared with  $h1$ , the  $U_{TSI}$  values with a 1s-average of  $h2$  and  $h3$  at the trackside location are increased by 3.3% and 7.6% respectively. Furthermore, the  $U_{TSI}$  values with a 1s-average at the platform location are increased by 1.6% and 3.0% respectively. According to the data in this section, the  $U_{TSI}$  values of 1s-average should be considered for the design of higher trains in the future to meet the safety of personnel besides the line.

### 3.3. Comparison of the wake flow

The previous content shows that the train height has an impact on the time-average slipstream. To better understand this phenomenon and reveal the flow characteristics around the train, the time-average streamline of the tail train surface is shown in Figure 16. The characteristic information of surface flow is represented by critical nodes, which contain saddle point  $SP$ , stable focus  $SF$ , and unstable node  $UN$ . The flow separation and adhesion processes are represented by the negative bifurcation line  $NBL$  and positive bifurcation line  $PBL$  respectively. Readers can refer to Dong et al. (2023) for more detailed information. Additionally, Figure 17 and Figure 19 also describe the specific spanwise vortex (SV) and longitudinal vortex (LV).

As shown in Figures 16–19, the streamlined length of the ICE3 model is close to 7 m. Therefore, large-scale flow separation rarely appears at the upper part of the tail nose,

only at the convex part of the cab window. The first air-flow separation happens near the cab window. When the airflow approaches  $NBL_1$  and  $NBL_2$ , it separates at high speed and forms longitudinal conical vortex  $LV_1$ . After that, the attached flow on the tail slope moves towards the centre due to the effect of the pressure gradient, and produces  $LV_2$  at  $NBL_3$  and  $NBL_4$ . Under the pressure suction caused by the separation of  $NBL_1$  and  $NBL_2$ ,  $LV_1$  and  $LV_2$  gradually move towards the ground and produce spanwise oscillation, as shown in Figure 18. The spatial streamlined form of  $LV_1$  and  $LV_2$  can be observed in Figure 19. This is similar to the three conical longitudinal vortices near the side of Ahmed's body proposed by Krajinović and Davidson (2005). Overall, the region between  $NBL_1$  and  $NBL_3$  is characterized by a large amount of reverse flow along the side surface of the window. With the upward movement of  $NBL_1$  contra-flow, it gradually spreads to  $NBL_3$  and separates.

Due to the influence of  $LV_1$  and  $LV_2$  longitudinal flow, the attached flow gradually spreads to the side and prompts the occurrence of the stable focus  $SF_1$  and  $SF_2$ . When approaching the tail nose, the airflow at  $NBL_5$  will separate induced by the severe reverse pressure gradient (Li et al., 2021). The airflow separated from  $NBL_5$  is attached to the inclined  $PBL_1$  at the lower part of the tail nose. Meanwhile, the airflow from the train bottom is separated at the  $NBL_6$ . It should be emphasized that the longitudinal vortices  $LV_3$  emerged from the train bottom and the cowcatcher is detected in this work, as shown in Figure 19. This phenomenon is similar to the wake flow of Dong et al. (2020), and is also similar to the separated wake structure at the cowcatcher presented by Xia et al.



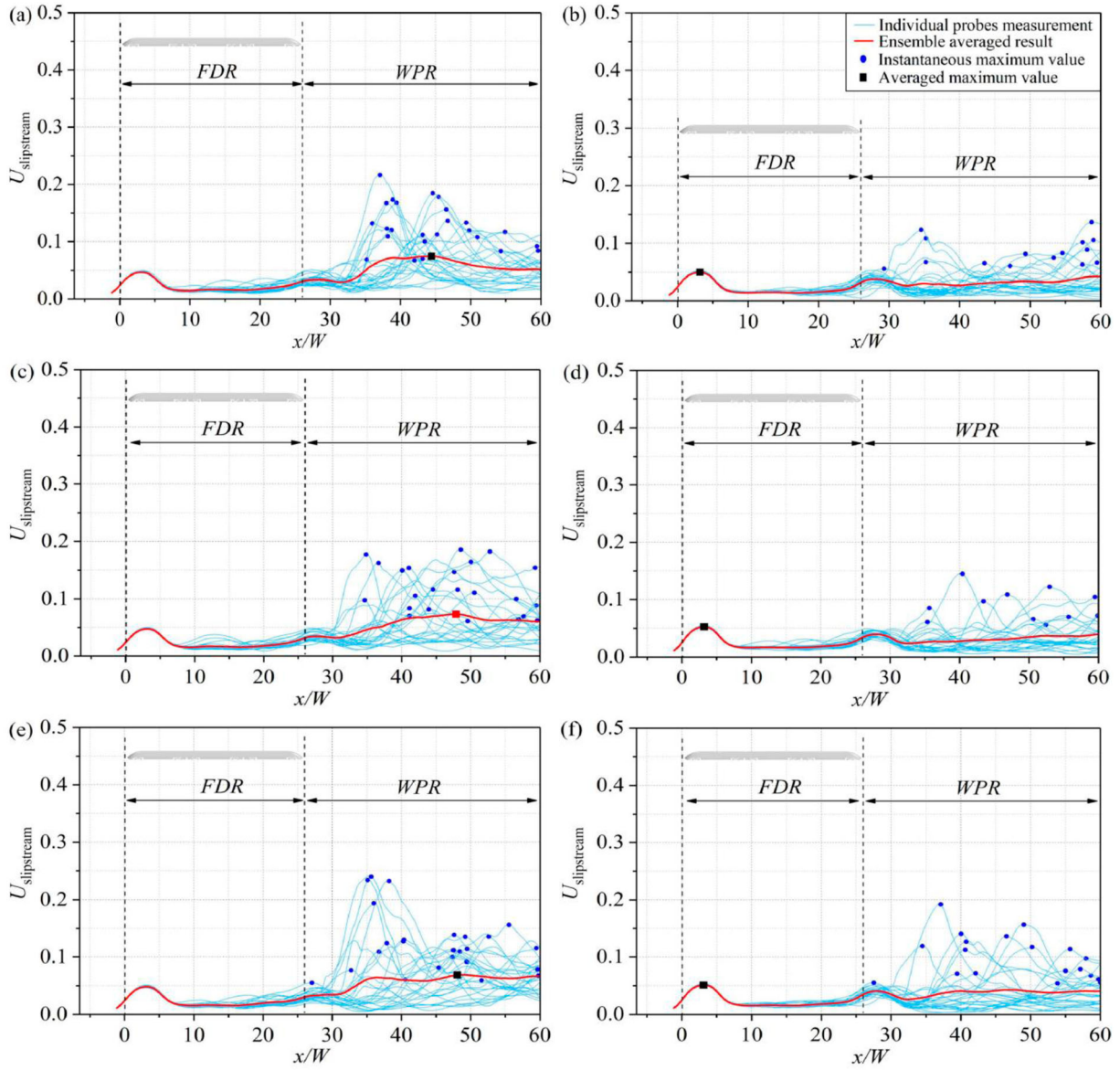


**Figure 15.** The 1s-average values of instantaneous slipstreams. *h1*: (a) trackside location and (b) platform location. *h2*: (c) trackside location and (d) platform location. *h3*: (e) trackside location and (f) platform location.

(2017). Of course, the bottom longitudinal flow often occurs in the case of Ahmed's body (Krajnović & Davidson, 2005; Siddiqui & Agelin-Chaab, 2022). Under the joint action of bottom longitudinal flow  $LV_3$  and negative bifurcation lines  $NBL_5$  and  $NBL_6$ , two spanwise vortices  $SV_1$  and  $SV_2$  are generated. As shown in Figure 16,  $SV_1$  and  $SV_2$  rotate in opposite directions and drive each other. The mirror symmetry of  $NBL_6$  about the centre of the train leads to the saddle point  $SP_1$ , and the unstable node  $UN_1$  on  $PBL_1$ . In addition, the central surface of the cowcatcher forms a radial stable node  $SN_1$  under the joint action of  $NBL_6$  and longitudinal flow  $LV_3$ . So far, the description of wake formation is complete.

The above description attempts to reveal the collective characteristics under three cases, while this section

**Table 5.** Amplitude statistics of the instantaneous slipstreams with or without the 1s-average method.

Locations	Train heights	Without 1s-average			With 1s-average		
		$\bar{U}_p$	$\sigma$	$U_{TSI}$	$\bar{U}_p$	$\sigma$	$U_{TSI}$
Trackside	<i>h1</i>	0.1785	0.0619	0.3023	0.1073	0.0342	0.1757
	<i>h2</i>	0.1878	0.0694	0.3266	0.1091	0.0360	0.1811
	<i>h3</i>	0.1971	0.0770	0.3511	0.1146	0.0371	0.1888
Platform	<i>h1</i>	0.1196	0.0354	0.1904	0.0680	0.0291	0.1262
	<i>h2</i>	0.1264	0.0467	0.2198	0.0694	0.0293	0.1280
	<i>h3</i>	0.1392	0.0487	0.2366	0.0706	0.0296	0.1298

focuses on the quantitative analysis of the impact of train height on the wake. Figure 17 shows the spanwise vortex structure in the WPR. The downwash angle of longitudinal flow  $LV_1$  and  $LV_2$  separated from the train side



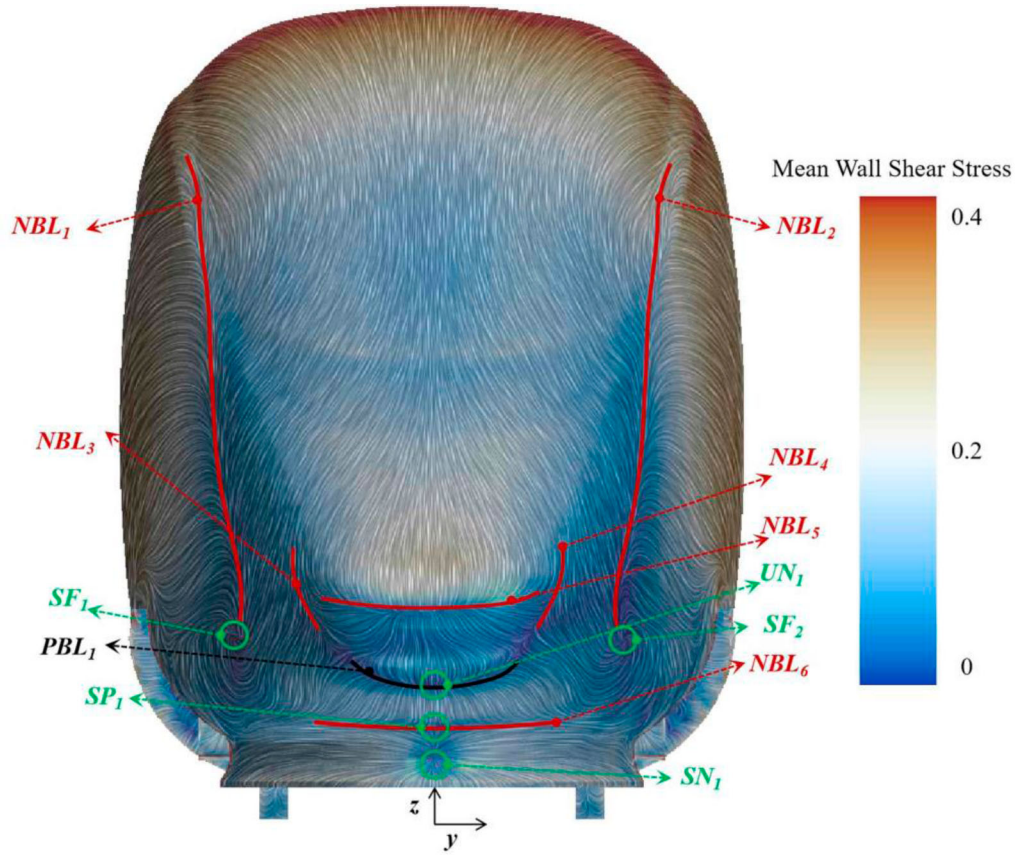


**Figure 16.** Surface flow diagram of the tail train. The train surface is coloured by the time-averaged wall shear stress.

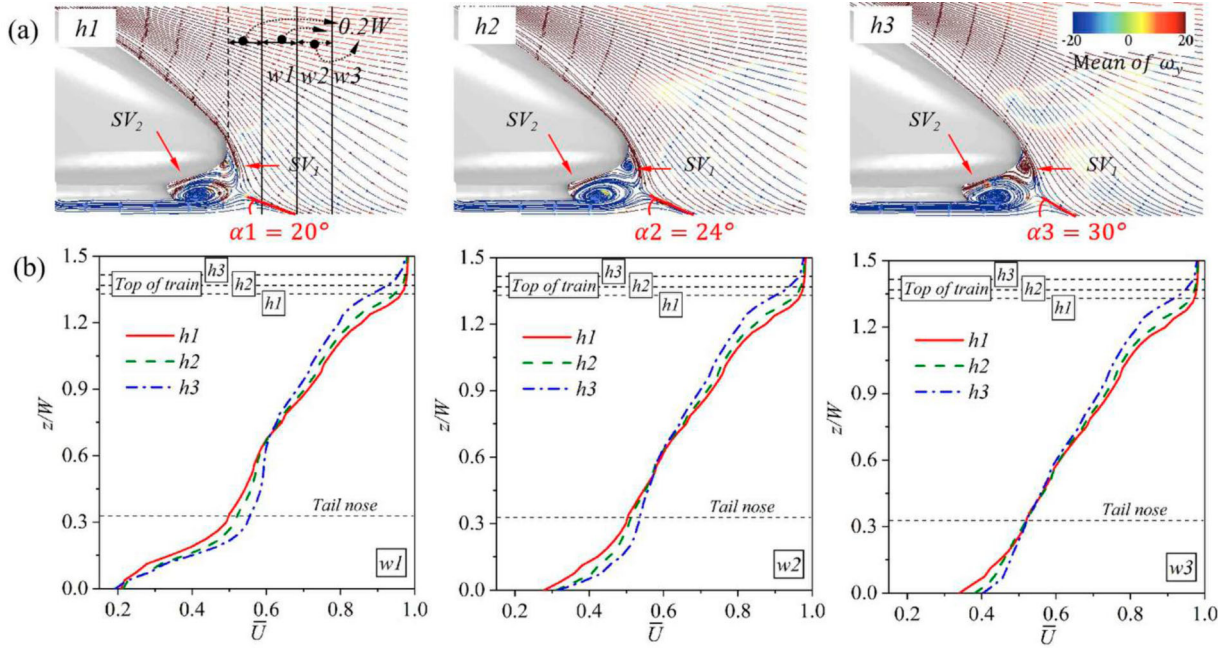


**Figure 17.** Spanwise vortices and velocity distribution in the WPR: (a) Spanwise vortices and (b) velocities sampled along vertical lines.

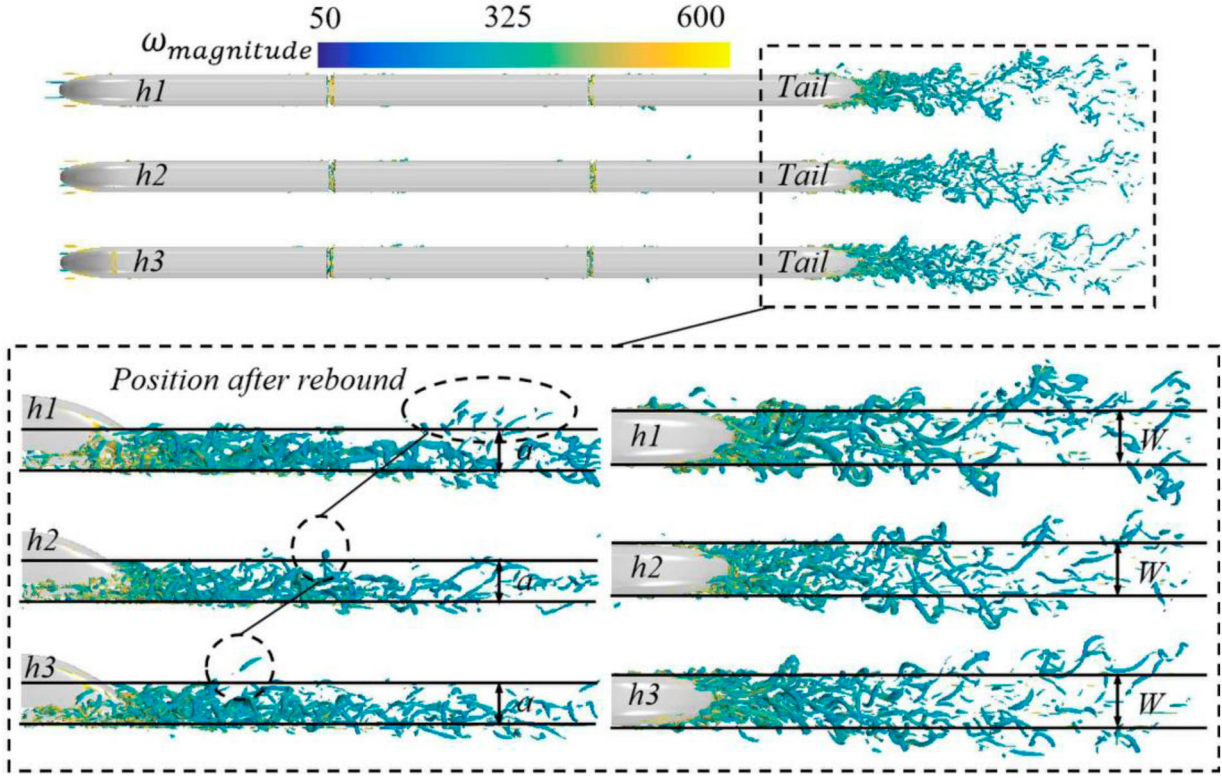


**Figure 18.** Instantaneous iso-surfaces coloured by vorticity magnitude ( $Q = 12000$ ). The photographs are recorded at  $350T_{inf}$ .

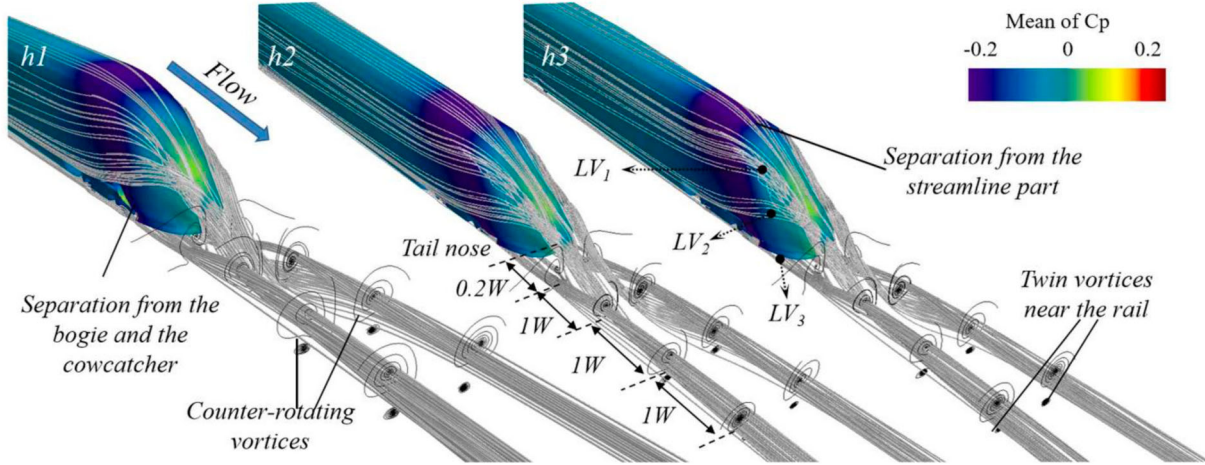


**Figure 19.** Spatial streamline at different train heights. The train is superimposed by the time-average pressure coefficient.

increases with the increasing slant angle, directly enhancing the vertical vorticity of spanwise vortices. It is found that the angles between downwash flow and ground flow ( $\alpha_1, \alpha_2, \alpha_3$ ) are  $20^\circ, 24^\circ$ , and  $30^\circ$  respectively, which represent the  $h1, h2$ , and  $h3$  cases. Meanwhile, the vorticity intensity of  $SV_1$  increases gradually. Additionally, Figure 17 (b) shows the velocity amplitude distribution along three vertical lines ( $w1, w2$ , and  $w3$ ). These sampling lines are located on the  $y = 0$  plane,  $0.2W, 0.4W$ , and  $0.6W$  from the tail nose. It can be observed that for the  $w1$  line, the speed gradually increases with the

increasing train height below  $0.7W$  height. This rule is the opposite when the height is greater than  $0.7W$ . Several factors could explain this observation. Firstly, with the increase in train height, the angle of downwash flow increases, which indirectly increases the speed of the lower part of the tail nose. Secondly, there is a certain blocking effect on the speed of the upper region with a higher train, resulting in a corresponding reduction in velocity. Additionally, the velocity of the  $w3$  acquisition line in the  $h3$  case is basically less than  $h1$ . It should be noted that the sum of velocity based on  $TF$  and slipstream



based on  $GF$  is 1. So this rule is consistent with the phenomenon in 3.2.1.

The instantaneous flow structures for the three train heights are shown in Figure 18. The iso-surface ( $Q = 12000$ ) is recorded by the visualized structure at  $T_{inf} = 350$  simulation time. The iso-surface is superimposed by vorticity amplitude. As mentioned above, the three longitudinal vortices and spanwise vortices separated from the tail train interfere with each other and develop downstream. The  $a = 0.8W$  in the side view and the train width is used to compare the iso-surface. With the increase in train height, the angle between downwash

flow and ground flow increases, making the wakes of  $h2$  and  $h3$  closer to the tail train. Meanwhile, the rebound location of the downwash flow is also closer to the tail nose, as presented in Figure 18. The wakes of the three cases show a small difference in width.

Figure 19 depicts a three-dimensional streamlined diagram around the tail train. The train surface is superimposed by the time-average pressure coefficient. As mentioned above, the longitudinal vortices separated from the side and bottom of the train are mixed with two spanwise vortices and then develop into two classical reverse rotation vortices. This wake structure is similar

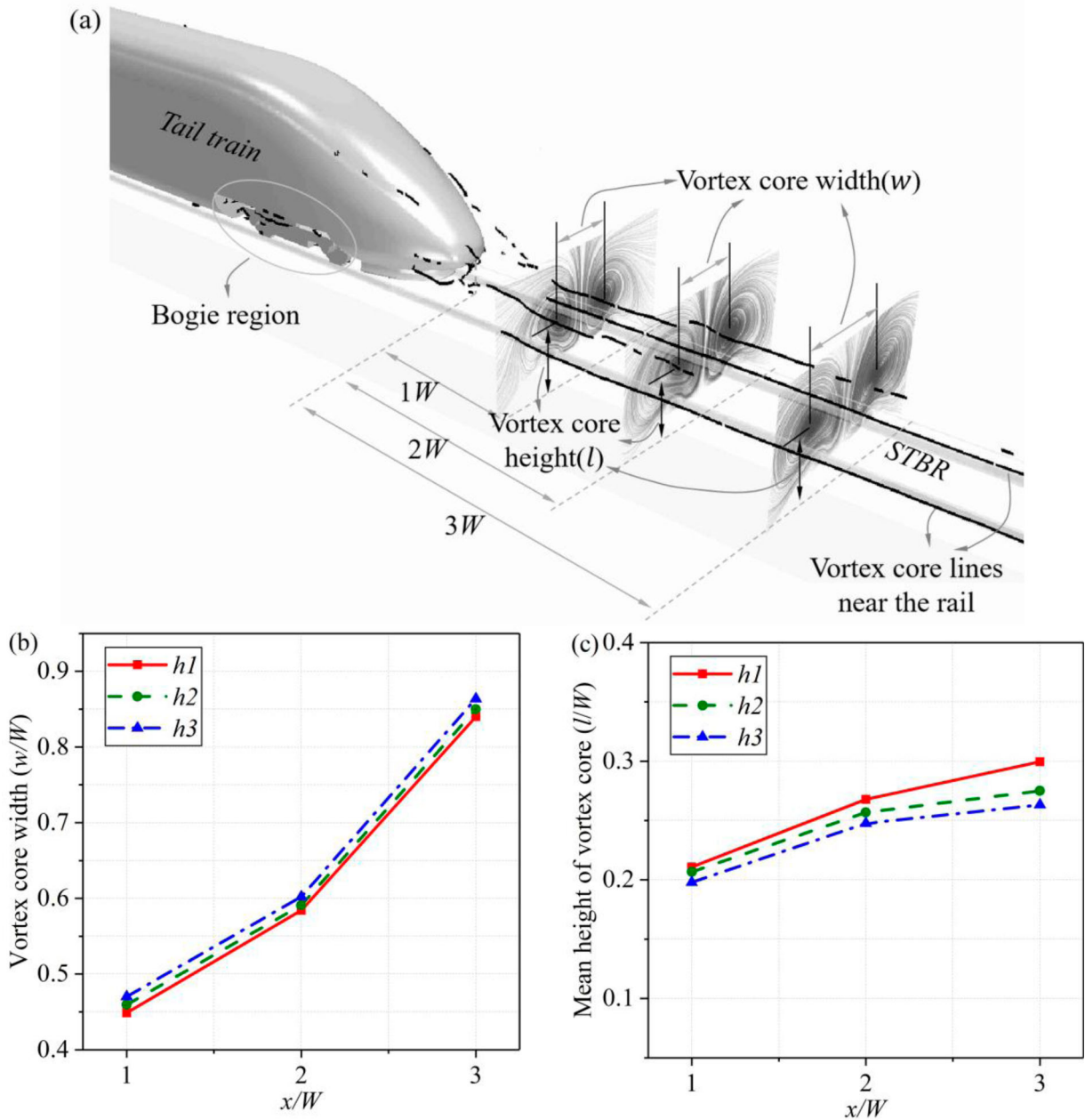


**Figure 20.** Spatial distribution of vortex cores: (a) The spatial distribution of the vortex cores and the cross-sectional tail streamlines; (b) variation of vortex core width with train height; (c) variation of the average height of vortex core with train height.



to that reported in previous research (Bell et al., 2017; Li et al., 2021). Moreover, we also found a pair of small vortices with reverse rotation on the outer side of the rail (as shown by the mark in Figure 19). This phenomenon was confirmed in the vortex core line in Figure 20. These vortex structures were also found in the previous research (Wang et al., 2020). Specific quantitative analysis will be shown below.

Figure 20 shows the position of the vortex core in WPR. It is found that numerous short vortex cores concentrate upon the bogie region. Additionally, the vortex core lines near the tail train confirm the existence and development of the above longitudinal flow  $LV_1$ ,  $LV_2$ , and  $LV_3$ . An interesting phenomenon is that there are two obvious vortex core lines along the rail. Meanwhile, the existence of the track has a certain locking-in effect on a pair of anti-rotating vortices in WPR, which can be also found in Figure 21. It should be emphasized that this research confirms the rail locking-in effect proposed by S. Wang et al., (2020) from the perspective of a vortex core line. To describe the vortex more intuitively, we use the concept of vortex core width and height to conduct

quantitative analysis. As shown in Figure 20, the widths of the vortex core on the  $x = 1W$ ,  $2W$ , and  $3W$  planes in the  $h3$  case are 4.5%, 3.0%, and 2.8% higher than that in the  $h1$  case, respectively. Meanwhile, the average vortex core heights on the  $x = 1W$ ,  $2W$ , and  $3W$  planes in the  $h3$  case are 6.5%, 8.1%, and 13.8% lower than that in the  $h1$  case, respectively. The results show that increasing the train height will produce a small diffusion of a slightly lower wake vortex in WPR, which will promote the outward and downward spread of the wake vortices.

To better understand the impact of train height on the evolution of vortex cores, Figure 21 describes the streamlined development process and quantitative analysis of the characteristic lengths of vortex cores. From Figure 21, the mixing process of  $LV_1$  and  $LV_3$  in the longitudinal flow occurs earlier, followed by the co-mixing of  $LV_1$  and  $LV_2$ , and  $LV_3$ . The fluid mixing position is marked with the black dotted line and red circle in the figure. The red circle represents the position of the second mixture and its distances from the tail nose and corresponding widths are used for subsequent comparison. From the

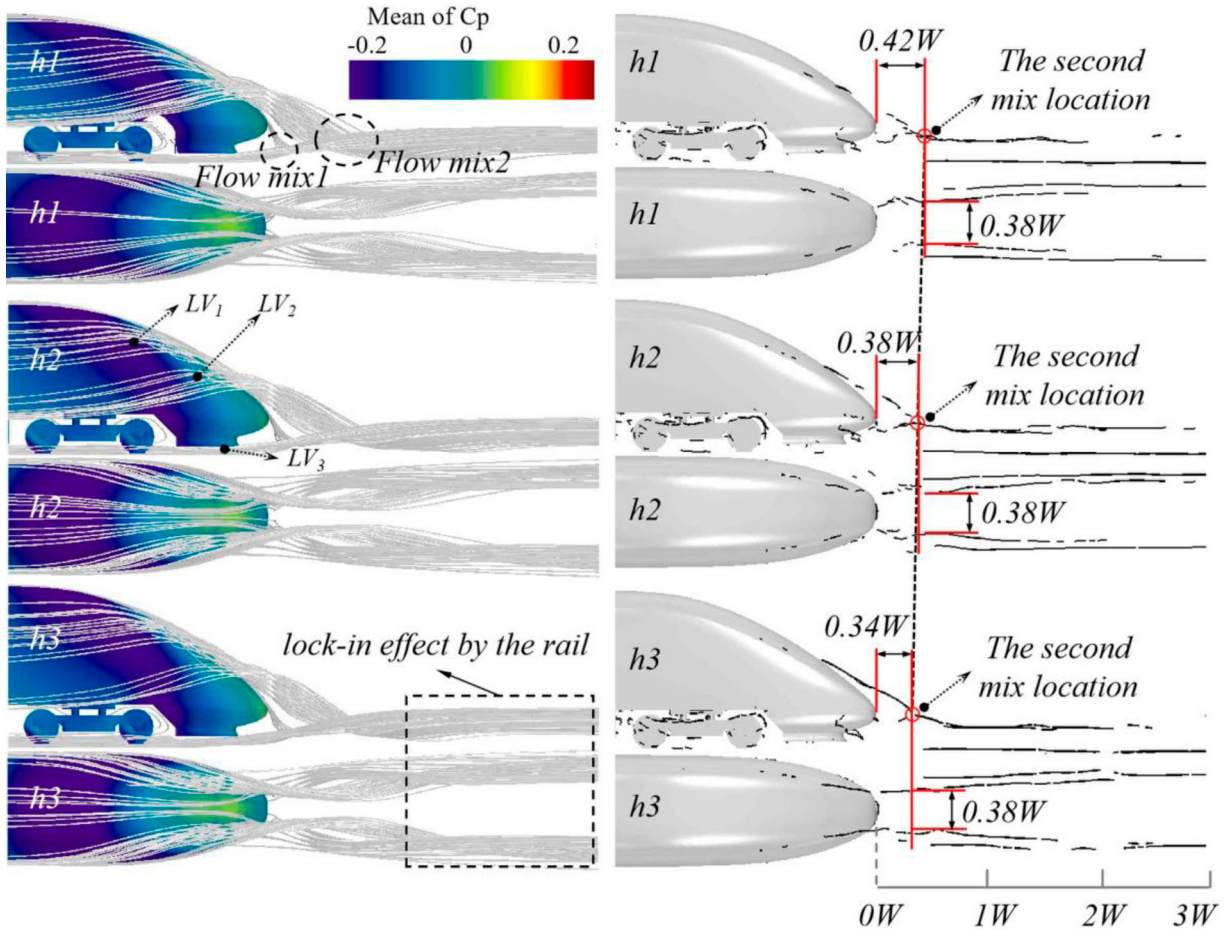


**Figure 21.** The development stage of the tail streamlines and quantitative analysis of the characteristic lengths of the vortex cores.

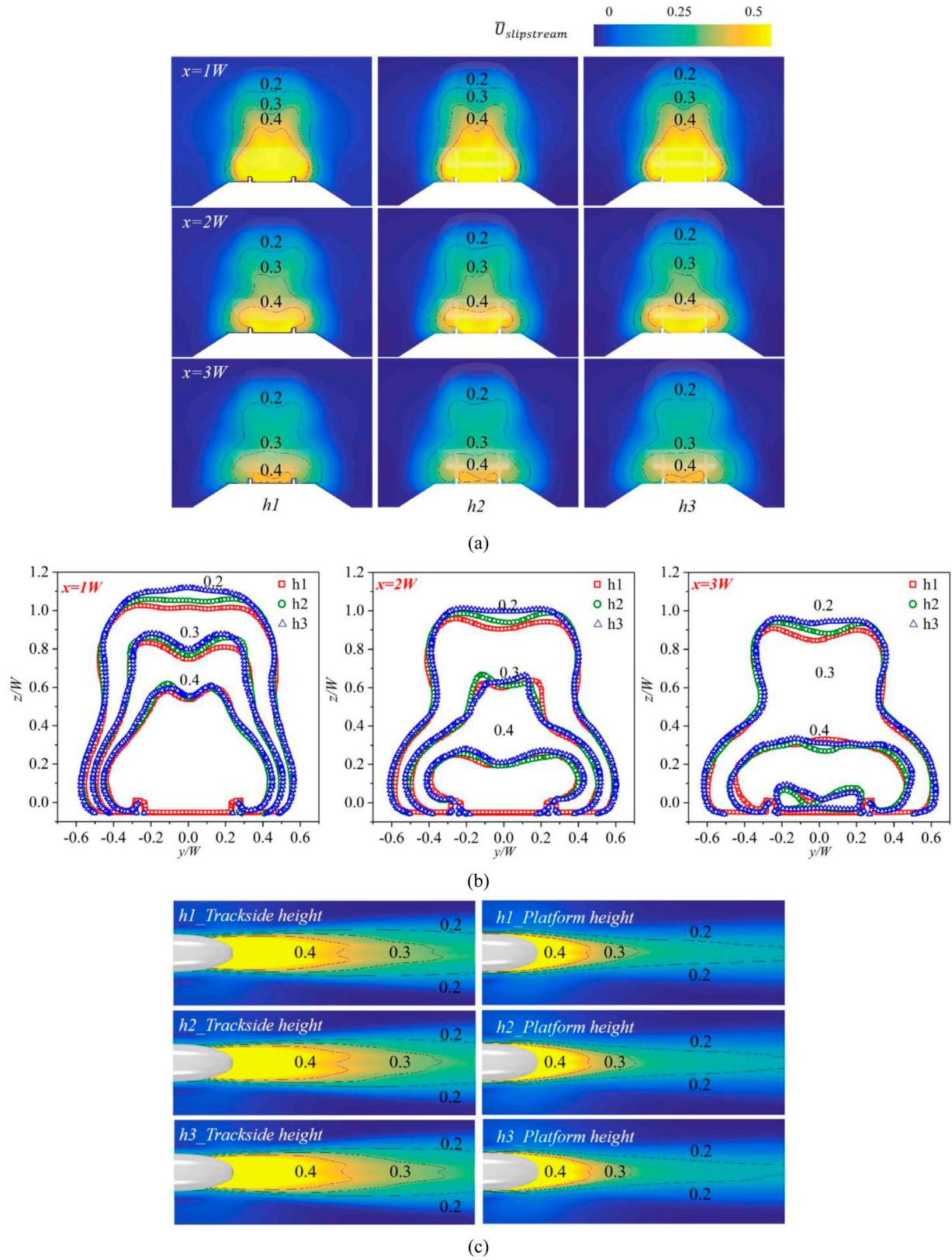


**Figure 22.** Distribution of mean slipstreams in three cases: (a) Comparison of slipstream velocities on three vertical planes in WPR, (b) comparison of slipstream isopleth (0.2, 0.3, and 0.4) in three cases, and (c) comparison of slipstream velocities in flow direction plane.

right column of Figure 21, it is seen that there are several stages in the development of the vortex core. First, the longitudinal flow  $LV_3$  is lifted near the tail nose and meets the longitudinal flow  $LV_1$ . After the first fluid mixing, the mixed flow of  $LV_3$  and  $LV_1$  continued to rise and mixed with  $LV_2$  for the second time at a short distance. After that, the mixed longitudinal flow gradually develops and spreads to both sides. However, under the locking-in effect of the rail, the trend of diffusion on both sides has weakened. With the increase of slant angle, the position of the second mixing gradually approaches the tail train. The spaces between the second mixing location and the tail nose are  $0.42W$ ,  $0.38W$ , and  $0.34W$  respectively, for  $h1$ ,  $h2$ , and  $h3$  cases. Additionally, the spanwise width of the mixing core at the second mixing location is also shown in the figure, which is consistent in all three cases. Therefore, the width of the vortex core is relatively larger at the same downstream location for  $h3$  due to diffusion. In general, the increase in train height will promote the occurrence of longitudinal flow mixing in advance, and then make it develop to wider sides.

Figure 22 shows the mean slipstream distributions on vertical planes ( $x = 1W$ ,  $x = 2W$ , and  $x = 3W$  from the tail nose). The slipstream velocity contours are used to compare three cases. In addition, the top views of slipstream distribution at the trackside location and platform location are also given. It is found that the high-speed slipstream is mainly concentrated in the rail in the spanwise direction, and mainly distributed between the ground and the tail nose in the vertical direction. As the vertical plane moves away from the tail train, the slipstream velocity value gradually decreases. From the slipstream velocity contours in Figure 22 (b), it indicates that the application of the higher trains may cause greater slipstream in influencing area  $WPR$ . It is also found that the mean slipstream in the stream-wise direction gradually decreases when moving away from the ground.

#### 4. Discussion

In this study, the time-averaged and TSI slipstreams are considered for the safety assessment of side flow near the

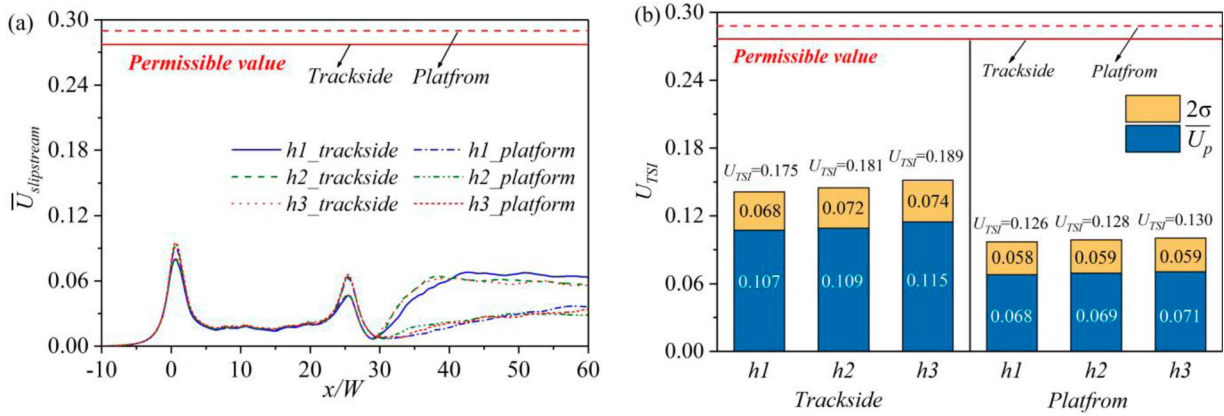


**Figure 23.** Safety analysis of CEN Standard for slipstream velocities: (a) Time-averaged slipstreams, and (b) TSI slipstreams with the 1s-average method.

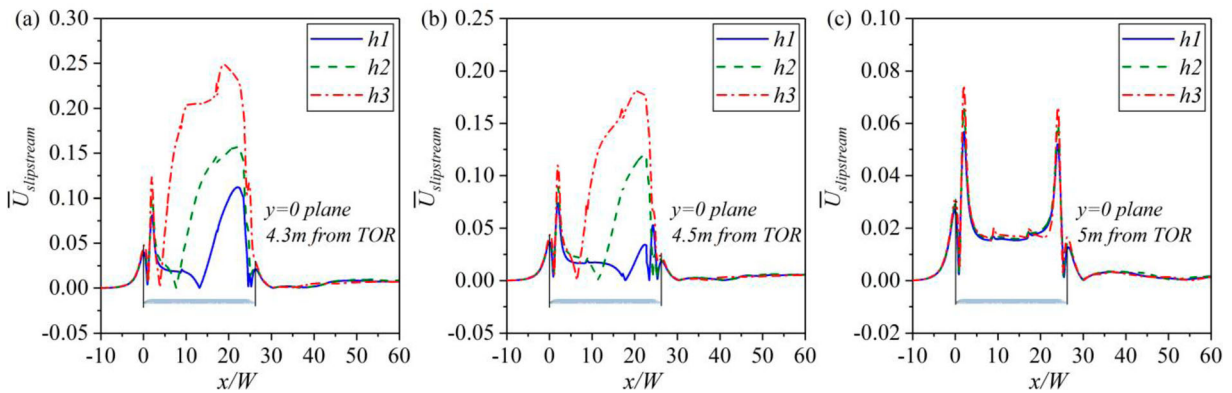


**Figure 24.** Comparison of time-averaged slipstreams on top of trains at  $y = 0$  plane for three cases: (a) 4.3 m (full scale) from the TOR, (b) 4.5 m from the TOR, and (c) 5 m from the TOR.



railway line. It can be seen from Figure 23 that the time-averaged and TSI slipstreams are far less than the limits of the CEN standard. However, with the increase in train height, the slipstreams have a small growth trend. This is more obvious for TSI slipstream without a 1s-average method. Besides, it can be observed in section 3.2.1 that a few instantaneous slipstreams exceed the standard limits. This means that under special circumstances, there may be a potential danger to people near the line and platform. Therefore, slipstream safety needs to be considered in the design stage of the higher trains.

Another region worthy of attention is the airflow at the top of the train, which may affect the electrical equipment above the train (such as the pantograph and catenary). Assuming that the height of the catenary is constant, the higher trains may bring a greater transient aerodynamic load to the above electrical equipment. As shown in Figure 24, at the same position located at the  $y = 0$  plane and 4.5 m away from TOR, the maximum time-averaged slipstream value of the *h3* case is 144% higher than that of the *h1* case. Therefore, if the higher trains are operating in the existing railway lines, it is recommended to shorten the maintenance period of electrical devices above the train to ensure equipment safety.

## 5. Conclusions

In the current work, the impact of train heights on the corresponding aerodynamic behaviours has been analyzed by using the IDDES method. The correctness of the calculation method is validated by the data measured from the wind tunnel test and moving model experiments. The above contents are summarized as follows.

- (1) The total drags of the train show an increasing trend when the train height increases. In the case of *h3*, the drag increases by 6.2% compared with the *h1* case. The change of lift is more sensitive than the drag, and the lift increases with the increasing train height. Compared with the *h1* case, the lift of the *h3* case increased by 23.8%. The influence of train height on aerodynamic force is also reflected in the frequency domain. The peak intensity and dominant frequency of force power spectral density show a downward trend with a higher train.
- (2) The height of the boundary layer near the train body is significantly raised by a higher train. Compared with the *h1* case, the maximum time-averaged slipstream velocities of *h2* and *h3* cases at the trackside location are increased by 1.0% and 2.4% respectively. Furthermore, the maximum time-averaged slipstream velocities at the platform location are

increased by 2.0% and 4.3% respectively. This indicates that higher trains will increase the potential risk to workers and infrastructure near the track.

- (3) The longitudinal vortices separate from the side of the tail train and the cowcatcher will merge with the spanwise vortices, then it develops downstream into twin anti-rotating vortices. The downwash angle of longitudinal flow at the train side gradually increases with the increasing slant angle. From *h1* to *h3*, the space between the vortex cores increases and the mean space between the vortex cores and the ground continues to decrease. This indicates that the higher train will force the wake to develop outward and downward, increasing the impact on the spanwise wake environment.
- (4) Compared with the *h1* case, the maximum time-average slipstream values of the *h2* and *h3* cases increased by 60% and 144% respectively at the same position located at the  $y = 0$  plane and 4.5 m away from the TOR. The operation of the higher trains will increase the transient aerodynamic load of equipment above the train, which also depends on the specific line parameters. It's recommended to shorten the maintenance period of electrical equipment above the train to ensure the safety of the devices.

In the current study, the discussion of the flow around the train is focused on the wake. In fact, the increase in the train height has an obvious impact on the pantograph region. In addition, the crosswind environment will bring greater challenges to the operation quality of the higher trains. Future research will mainly focus on the impact of train heights on dynamic stability and flow fields near pantographs in crosswind environments. Besides, the current work uses 3-car formation trains. Usually, the length of a train has a certain impact on the slipstream in the tail train and wake region. To provide real aerodynamic parameters for the design of the higher trains, it is necessary to further study the impact of train formation length on aerodynamic characteristics in the future.

## Acknowledgments

The authors acknowledge the computational resources provided by the High-Performance Computing Centre of Central South University, China.

## Disclosure statement

No potential conflict of interest was reported by the author(s).

## Data availability

The data that supports the findings of this study are available from both the first author and the corresponding author upon reasonable request.

## Funding

This work was supported by the National Key R&D Program of China (Grant No. 2020YFA0710903); the Natural Science Foundation of Hunan Province (Grant No. 2021JJ30849); the Graduate Student Independent Innovation Project of Hunan Province (Grant No. CX20200196); the Graduate Student Independent Innovation Project of Central South University (Grant Nos. 2020zzts111 and 2020zzts117).

## ORCID

Xiaohui Xiong  <http://orcid.org/0000-0002-0406-5237>

## References

- Aschwandten, P., Müller, J., Travaglio, G. C., & Schöning, T. (2009). The influence of motion aerodynamics on the simulation of vehicle dynamics. *SAE International Journal of Passenger Cars - Mechanical Systems*, 1(1), 545–551. <https://doi.org/10.4271/2008-01-0657>
- Baker, C. J., Quinn, A., Sima, M., Hoefener, L., & Licciardello, R. (2014a). Full-scale measurement and analysis of train slipstreams and wakes. Part 1: Ensemble averages. *Proceedings of the Institution of Mechanical Engineers, Part F: Journal of Rail and Rapid Transit*, 228(5), 451–467. <https://doi.org/10.1177/0954409713485944>
- Baker, C. J., Quinn, A., Sima, M., Hoefener, L., & Licciardello, R. (2014b). Full-scale measurement and analysis of train slipstreams and wakes. Part 2 gust analysis. *Proceedings of the Institution of Mechanical Engineers, Part F: Journal of Rail and Rapid Transit*, 228(5), 468–480. <https://doi.org/10.1177/0954409713488098>
- Bell, J. R., Burton, D., Thompson, M. C., Herbst, A. H., & Sheridan, J. (2015). Moving model analysis of the slipstream and wake of a high-speed train. *Journal of Wind Engineering and Industrial Aerodynamics*, 136, 127–137. <https://doi.org/10.1016/j.jweia.2014.09.007>
- Bell, J. R., Burton, D., Thompson, M. C., Herbst, A. H., & Sheridan, J. (2017). The effect of tail geometry on the slipstream and unsteady wake structure of high-speed trains. *Experimental Thermal and Fluid Science*, 83, 215–230. <https://doi.org/10.1016/j.expthermflusci.2017.01.014>
- Boufferrouk, A. (2013). Methods of calculating aerodynamic force on a vehicle subject to turbulent crosswinds. *American Journal of Fluid Dynamics*, 3(34), 119–134. <https://doi.org/10.5923/j.ajfd.20130304.04>
- CEN European Standard. (2013). Railway applications–aerodynamics-Part4: requirements and test procedures for aerodynamics on open track. TSI/EN 14067-4.
- Cheng, F., Xiong, X. H., Tang, M. Z., Li, X. B., & Wang, X. R. (2022). Impact of the gap distance between two adjacent external windshields of a high-speed train on surrounding flow characteristics: An IDDES study. *Engineering Applications of Computational Fluid Mechanics*, 16(1), 724–745. <https://doi.org/10.1080/19942060.2022.2046168>
- Dong, T., Minelli, G., Wang, J., Liang, X., & Krajnović, S. (2020). The effect of ground clearance on the aerodynamics of a generic high-speed train. *Journal of Fluids and Structures*, 95, 102990. <https://doi.org/10.1016/j.jfluidstructs.2020.102990>
- Dong, X., Li, Y., Cai, T., Zhou, W., Cai, X., & Dong, Y. (2023). Quantitative experimental research on vortex generation and self-maintenance mechanisms in turbulence. *Physics of Fluids*, 35(05), 055118. <https://doi.org/10.1063/5.0142624>
- Ehirim, O. H., Knowles, K., & Saddington, A. J. (2019). A review of ground-effect diffuser aerodynamics. *Journal of Fluids Engineering*, 141(2), 1–19. <https://doi.org/10.1115/1.4040501>
- François, D. G., Delnero, J. S., Colman, J., Marañón Di Leo, J., & Camocardi, M. E. (2009). Experimental determination of stationary aerodynamics loads on a double deck bus. *11th Americas Conference on Wind Engineering*.
- Guo, Z., Liu, T., Hemida, H., Chen, Z., & Liu, H. (2020). Numerical simulation of the aerodynamic characteristics of double unit train. *Engineering Applications of Computational Fluid Mechanics*, 14(1), 910–922. <https://doi.org/10.1080/19942060.2020.1784798>
- Hemida, H., Gil, N., & Baker, C. (2010). LES of the slipstream of a rotating train. *Journal of Fluids Engineering*, 132(5), 0511031. <https://doi.org/10.1115/1.4001447>
- Krajnović, S., & Davidson, L. (2005). Flow around a simplified car, part 2: Understanding the flow. *Journal of Fluids Engineering*, 127(5), 919–928. <https://doi.org/10.1115/1.1989372>
- Li, X. B., Chen, G., Liang, X. F., Liu, D. R., & Xiong, X. H. (2021). Research on spectral estimation parameters for application of spectral proper orthogonal decomposition in train wake flows. *Physics of Fluids*, 33(12), 125103. <https://doi.org/10.1063/5.0070092>
- Liu, H., Zhang, S., Liang, X., & Zou, Y. (2022). The effect of covering structure in pantograph sinking platform on the aerodynamics of high-speed train. *Engineering Applications of Computational Fluid Mechanics*, 16(1), 2157–2175. <https://doi.org/10.1080/19942060.2022.2133517>
- Masson, E., Paradot, N., & Allain, E. (2012). Notes on numerical fluid mechanics and multidisciplinary design. *Noise and Vibration Mitigation for Rail Transportation Systems*, 118(5), 437–444. [https://doi.org/10.1007/978-4-431-53927-8\\_52](https://doi.org/10.1007/978-4-431-53927-8_52)
- Mohrfeld-Halterman, J. A., & Uddin, M. (2016). Quasi steady-state aerodynamic model development for race vehicle simulations. *Vehicle System Dynamics*, 54(1), 124–136. <https://doi.org/10.1080/00423114.2015.1131840>
- Muld, T. W., Efraimsson, G., & Henningson, D. S. (2014). Wake characteristics of high-speed trains with different lengths. *Proceedings of the Institution of Mechanical Engineers, Part F: Journal of Rail and Rapid Transit*, 228(4), 333–342. <https://doi.org/10.1177/0954409712473922>
- Niu, J., Wang, Y., Zhang, L., & Yuan, Y. (2018). Numerical analysis of aerodynamic characteristics of high-speed train with different train nose lengths. *International Journal of Heat and Mass Transfer*, 127, 188–199. <https://doi.org/10.1016/j.ijheatmasstransfer.2018.08.041>
- Paradot, N., & Bouchet, J. P. (2009). Determination of aerodynamic coefficients of the TGV Duplex in wind tunnel for flat ground configurations. *EuroMech colloquium 509, Vehicle Aerodynamics*, Berlin, Germany.
- Raghunathan, R. S., Kim, H. D., & Setoguchi, T. (2002). Aerodynamics of high-speed railway train. *Progress in Aerospace Sciences*, 38(6), 469–514. [https://doi.org/10.1016/S0376-0421\(02\)00029-5](https://doi.org/10.1016/S0376-0421(02)00029-5)

- Siddiqui, N. A., & Agelin-Chaab, M. (2022). Experimental investigation of the flow features around an elliptical Ahmed body. *Physics of Fluids*, 34(10), 105119. <https://doi.org/10.1063/5.0114377>
- Tan, C., Zhou, D., Chen, G., Sheridan, J., & Krajnovic, S. (2020). Influences of marshalling length on the flow structure of a maglev train. *International Journal of Heat and Fluid Flow*, 85(6), 108604. <https://doi.org/10.1016/j.ijheatfluidflow.2020.108604>
- Tian, H. (2019). Review of research on high-speed railway aerodynamics in China. *Transportation Safety and Environment*, 1(1), 1–21. <https://doi.org/10.1093/tse/tdz014>
- Wang, F., Weng, M., Xiong, K., Han, J., Obadi, I., & Liu, F. (2022). Study on aerodynamic pressures caused by double-train tracking operation in a metro tunnel. *Tunnelling and Underground Space Technology*, 123(11), 104434. <https://doi.org/10.1016/j.tust.2022.104434>
- Wang, J., Gao, G., Li, X., Liang, X., & Zhang, J. (2020). Effect of bogie fairings on the flow behaviours and aerodynamic performance of a high-speed train. *Vehicle System Dynamics*, 58(6), 890–910. <https://doi.org/10.1080/00423114.2019.1607400>
- Wang, S., Burton, D., Herbst, A., Sheridan, J., & Thompson, M. C. (2018). The effect of bogies on high-speed train slipstream and wake. *Journal of Fluids and Structures*, 83, 471–489. <https://doi.org/10.1016/j.jfluidstructs.2018.03.013>
- Wang, S., Burton, D., Herbst, A. H., Sheridan, J., & Thompson, M. C. (2020). The impact of rails on high-speed train slipstream and wake. *Journal of Wind Engineering and Industrial Aerodynamics*, 198(2), 104114. <https://doi.org/10.1016/j.jweia.2020.104114>
- Xia, C., Wang, H., Shan, X., Yang, Z., & Li, Q. (2017). Effects of ground configurations on the slipstream and near wake of a high-speed train. *Journal of Wind Engineering and Industrial Aerodynamics*, 168(6), 177–189. <https://doi.org/10.1016/j.jweia.2017.06.005>
- Xia, Y., Liu, T., Gu, H., Guo, Z., Chen, Z., Li, W., & Li, L. (2020). Aerodynamic effects of the gap spacing between adjacent vehicles on wind tunnel train models. *Engineering Applications of Computational Fluid Mechanics*, 14(1), 835–852. <https://doi.org/10.1080/19942060.2020.1773319>
- Zou, S., He, X., Hu, L., Wang, H., & Kareem, A. (2022). Characteristics of the velocity field in slipstream induced by a CR 400 high-speed train lead-carriage. *Measurement*, 196(4), 111205. <https://doi.org/10.1016/j.measurement.2022.111205>